

# Deducing transport properties of mobile vacancies from perovskite solar cell characteristics

EP

Cite as: J. Appl. Phys. 128, 184501 (2020); doi: 10.1063/5.0021849

Submitted: 15 July 2020 · Accepted: 14 October 2020 ·

Published Online: 9 November 2020



View Online



Export Citation



CrossMark

James M. Cave,<sup>1</sup> Nicola E. Courtier,<sup>2</sup> Isabelle A. Blakborn,<sup>3,a)</sup> Timothy W. Jones,<sup>3</sup> Dibyajyoti Ghosh,<sup>4,b)</sup> Kenrick F. Anderson,<sup>3</sup> Liangyou Lin,<sup>3,c)</sup> Andrew A. Dijkhoff,<sup>3,a)</sup> Gregory J. Wilson,<sup>3</sup> Krishna Feron,<sup>3,d)</sup> M. Saiful Islam,<sup>4</sup> Jamie M. Foster,<sup>5</sup> Giles Richardson,<sup>2</sup> and Alison B. Walker<sup>1,e)</sup>

## AFFILIATIONS

<sup>1</sup>Department of Physics, University of Bath, Bath BA2 7AY, United Kingdom<sup>2</sup>Mathematical Sciences, University of Southampton, Southampton SO17 1BJ, United Kingdom<sup>3</sup>CSIRO Energy, Newcastle Energy Centre, 10 Murray Dwyer Circuit, Mayfield West, NSW 2304, Australia<sup>4</sup>Department of Chemistry, University of Bath, Bath BA2 7AY, United Kingdom<sup>5</sup>Department of Mathematics, University of Portsmouth, Portsmouth PO1 3HF, United Kingdom<sup>a)</sup>**Also at:** Faculty of Applied Sciences, Delft University of Technology, 2628 CJ Delft, The Netherlands.<sup>b)</sup>**Also at:** Department of Physics, University of Bath, Bath BA2 7AY, United Kingdom. **Present address:** Theoretical Division, Los Alamos National Laboratory, Los Alamos, NM 87545, USA.<sup>c)</sup>**Also at:** School of Materials Science and Engineering, Huazhong University of Science & Technology, Wuhan 430074, China.<sup>d)</sup>**Also at:** Centre for Organic Electronics, University of Newcastle, NSW 2308, Australia.<sup>e)</sup>**Author to whom correspondence should be addressed:** a.b.walker@bath.ac.uk

## ABSTRACT

The absorber layers in perovskite solar cells possess a high concentration of mobile ion vacancies. These vacancies undertake thermally activated hops between neighboring lattice sites. The mobile vacancy concentration  $N_0$  is much higher and the activation energy  $E_A$  for ion hops is much lower than is seen in most other semiconductors due to the inherent softness of perovskite materials. The timescale at which the internal electric field changes due to ion motion is determined by the vacancy diffusion coefficient  $D_v$  and is similar to the timescale on which the external bias changes by a significant fraction of the open-circuit voltage at typical scan rates. Therefore, hysteresis is often observed in which the shape of the current-voltage, J-V, characteristic depends on the direction of the voltage sweep. There is also evidence that this defect migration plays a role in degradation. By employing a charge transport model of coupled ion-electron conduction in a perovskite solar cell, we show that  $E_A$  for the ion species responsible for hysteresis can be obtained directly from measurements of the temperature variation of the scan-rate dependence of the short-circuit current and of the hysteresis factor  $H$ . This argument is validated by comparing  $E_A$  deduced from measured J-V curves for four solar cell structures with density functional theory calculations. In two of these structures, the perovskite is MAPbI<sub>3</sub>, where MA is methylammonium, CH<sub>3</sub>NH<sub>3</sub>; the hole transport layer (HTL) is spiro (spiro-OMeTAD, 2,2',7,7'- tetrakis[N,N-di(4-methoxyphenyl) amino]-9,9'-spirobifluorene) and the electron transport layer (ETL) is TiO<sub>2</sub> or SnO<sub>2</sub>. For the third and fourth structures, the perovskite layer is FAPbI<sub>3</sub>, where FA is formamidinium, HC(NH<sub>2</sub>)<sub>2</sub>, or MAPbBr<sub>3</sub>, and in both cases, the HTL is spiro and the ETL is SnO<sub>2</sub>. For all four structures, the hole and electron extracting electrodes are Au and fluorine doped tin oxide, respectively. We also use our model to predict how the scan rate dependence of the power conversion efficiency varies with  $E_A$ ,  $N_0$ , and parameters determining free charge recombination.

Published under license by AIP Publishing. <https://doi.org/10.1063/5.0021849>

## I. INTRODUCTION

Perovskite solar cells (PSCs) have generated intense research interest since the power conversion efficiencies (PCEs) of laboratory cells now match those of the best established inorganic polycrystalline technologies due to the rapid rise in the PCE, and they are easy to prepare in the laboratory through low-temperature solution processing<sup>1,2</sup> due to their soft nature.<sup>3,4</sup> Other advantages include high absorptivity and excellent carrier diffusion lengths.<sup>5</sup>

Recent studies, for example, electro-absorption measurements,<sup>6</sup> multidimensional luminescence imaging,<sup>7</sup> and transfer curves and output curves of perovskite field effect transistors,<sup>8</sup> have demonstrated that the ion motion occurs in perovskite devices. The ion motion can be beneficial, such as in memristors,<sup>9</sup> and it can enhance the PSC performance.<sup>10</sup> While mobile ions are not always associated with less stable devices, they have been shown to impose constraints on cell performance and stability assessment<sup>11</sup> and can result in a lower efficiency with the same concentration of defects compared to the same device without mobile ions.<sup>12</sup> Furthermore, vacancy migration accelerates non-radiative charge recombination by inducing lattice distortions,<sup>13</sup> and perovskite layers and their interfaces with transport layers are degraded by the strain in the perovskite lattice.<sup>14</sup>

In standard measurements of hysteresis, a reverse scan, which sweeps the applied bias from just above the open-circuit voltage ( $V_{oc}$ ) to zero volts, is followed by a forward scan, taking the applied bias from zero volts [at which the short-circuit current density ( $J_{sc}$ ) is measured] to the voltage at the start of the reverse scan. For a given applied bias, the currents measured on the reverse scan are greater (normal hysteresis) or less (inverted hysteresis<sup>15</sup>) than those measured on the forward scan. To quantify these effects, the hysteresis factor  $H = (A_{rev} - A_{for})/A_{rev}$ , where  $A_{rev}$  and  $A_{for}$  are the areas under the current–voltage (J–V) curve for the reverse and forward scan, respectively, is used. The hysteresis observed in our cells is the normal kind in which  $A_{rev} > A_{for}$  (so that  $H > 0$ ), however, inverse or mixed hysteresis is also possible, and in such cases, the definitions suggested by Nemnes *et al.*<sup>16</sup> may be more appropriate. The hysteresis factor  $H$  is

important because it can be used to infer the timescales associated with the defect motion. In particular, it takes its largest values at scan rates where changes in the internal field due to change in bias are comparable to internal field changes from the ion motion over the same time period. Cell characteristics, such as  $H$ , that encapsulate kinetic effects should be used with care because of their sensitivity to scan speed,<sup>17,18</sup> scan range, scan direction, prebiasing, and temperature.<sup>19</sup>

It is also important to note that  $A_{rev}$  and  $A_{for}$  do not measure the power generated during those scans since a J–V curve describes a locus of operational states.

A PSC structure and its operation are shown in Fig. 1(a). Measured J–V curves at varying scan rates and temperatures are reported here for four PSC structures labeled A, B, C and D. In structures A and B, the light harvesting layer is  $\text{MAPbI}_3$  (MAPI); in structure C, it is  $\text{FAPbI}_3$  (FAPI); and in structure D, it is  $\text{MAPbBr}_3$  (MAPBr). For these perovskites, the organic cation is methylammonium (MA,  $\text{CH}_3\text{NH}_3$ ) or formamidinium [FA,  $\text{HC}(\text{NH}_2)_2$ ]. In all four PSC architectures, the hole transport layer (HTL) is spiro (spiro-OMeTAD, 2,2',7,7'-tetrakis[N,N-di(4-methoxyphenyl)amino]-9,9'-spirobifluorene). The electron transport layer (ETL) is  $\text{TiO}_2$  in structure a, and  $\text{SnO}_2$  for the other structures. In all four structures, the hole and electron extracting electrodes are Au and FTO (fluorine doped tin oxide), respectively.

For perovskites, Schottky defects dominate. These defects are unoccupied anion and cation sites in a stoichiometric ratio and are randomly distributed in a crystal in equilibrium. At full Schottky disorder, the unoccupied anion sites are positively charged iodide vacancies,  $\text{V}_I^+$ , and unoccupied cation sites are negatively charged MA vacancies,  $\text{V}_{MA}^-$ , and Pb vacancies,  $\text{V}_{Pb}^-$ .<sup>20</sup> Density functional theory (DFT) calculations for MAPI predict a low Schottky formation energy per defect  $E_V$  of 0.14 eV,<sup>20</sup> consistent with 0.1–0.2 eV reported by Tong *et al.*<sup>21</sup> At room temperature, the  $\text{V}_I^+$  concentration  $N_0 = 0.4\% = 1.6 \times 10^{19} \text{ cm}^{-3}$  for a cubic unit cell with lattice constant  $a = 0.628 \text{ nm}$ .<sup>22,23</sup> Eames *et al.*<sup>22</sup> estimated  $E_A$  for  $\text{V}_I^+$  as 0.58 eV for cubic MAPI (similar to the more recent value of

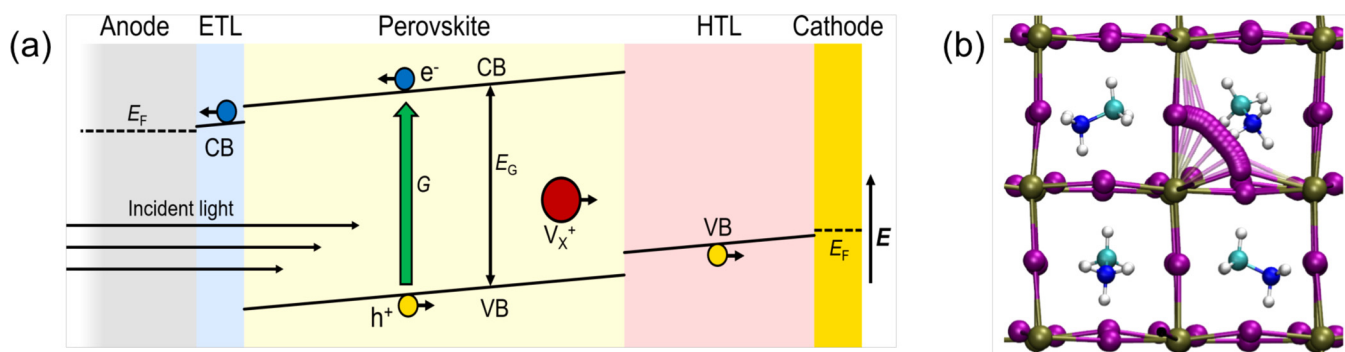


**FIG. 1.** (a) The planar PSC structure. Its material composition for structures A to D is defined in the text. The simulated ETL, perovskite layer, and HTL thicknesses for the four device architectures, whose measured and modeled characteristics are reported in this paper, are 50 nm, 400 nm, and 200 nm, respectively. The green vertical arrow shows generation of electrons ( $e^-$ , blue disks) and holes ( $h^+$ , yellow disks) through light absorption in the perovskite layer. Carriers are then transported as shown by horizontal arrows to the carrier-selective, electron and hole, transport layers (ETL and HTL, respectively) and from there into the electrodes. Conduction and valence bands (CB and VB), the bandgap  $E_g$ , Fermi levels ( $E_F$ ), and a halide vacancy ( $V_X^+$ , red disk) are shown. (b) Migration path of  $\text{I}^-$  vacancy in MAPI from our DFT simulations. The color scheme is purple,  $\text{I}^-$ ; dark blue, N; cyan, C; white, H; and brown, Pb.

0.55 eV<sup>24</sup>). They find a much higher  $E_A$  of 0.84 eV for  $V_{MA}^-$  migration, given that its path is through the unit cell face or through a bottleneck comprising four  $I^-$  ions, and  $E_A$  of 2.31 eV for  $V_{Pb}^-$ , suggesting an immobile Pb sublattice.

We have predicted the  $V_I^+$  trajectory between adjacent lattice sites in tetragonal MAPI, shown in Fig. 1(b) and note that it is similar in shape to the path reported by Eames *et al.*<sup>22</sup> The diffusion coefficient of ion vacancies  $D_v$  has an Arrhenius dependence on temperature  $T$ ,  $D_v = D_{v\infty} \exp(-E_A/k_B T) = 2 \times 10^{-13} \text{ cm}^2/\text{s}$  at room temperature for  $E_A = 0.58 \text{ eV}$ . Here, the high temperature ion diffusion coefficient  $D_{v\infty} = a^2 f_a / 12 = 3 \times 10^{-4} \text{ cm}^2 \text{ s}^{-1}$ , where  $f_a = 1 \text{ THz}$  is the hop attempt frequency.

To see hysteresis in J-V scans, the timescale at which the ion motion influences fields within the perovskite layer should be comparable to the time taken by the J-V scan as measured by the scan rate. The ion motion causes local accumulation of space charge in narrow layers termed Debye layers. For experimental measurements of J-V curves,  $V_I^+$  is the only species whose migration occurs on the relevant timescales. The Debye layer created by accumulation of  $V_I^+$  next to the HTL has width  $L_D \approx 2 \text{ nm}$  using parameter values in Table II of the [supplementary material](#). A second wider Debye layer next to the ETL arises from  $V_I^+$  depletion.<sup>19,22,23,25–27</sup> The Debye layers alter the electrostatic potential profile, which is not significantly affected by the free charge carriers whose concentration, even at the maximum value at open circuit, is four orders of magnitude lower than  $N_0$ .

The following argument<sup>28</sup> gives a rough estimate for these timescales. The ion mobility deduced from  $D_v$  for  $V_I^+$  using the Einstein relation gives a drift velocity of  $2 \times 10^{-7} \text{ cm/s}$  at short circuit, assuming a field of  $V_{oc}/b$ , where  $b = 400 \text{ nm}$  is the perovskite layer width. Therefore, it takes about 1 s for ions to move a distance equal to  $L_D$  and hence for charge to be transferred between the two perovskite Debye layers due to all mobile ions moving an average distance of one Debye length. This timescale is consistent with maximum hysteresis occurring at scan rates of around a few

hundred mV/s and with the low frequency semicircles observed in Nyquist plots of impedance measurements. These semicircles can be interpreted as arising from modifications in the rate of charge recombination caused by ion transport.<sup>28</sup>

Timescales of around 6 h have been associated with the motion of the methylammonium vacancy  $V_{MA}^-$ ,<sup>14</sup> and since these are much greater than the timescales observed in our measurements, we do not explicitly model the motion of such defects, instead modeling them as uniformly distributed static background counter charge.

The effects of ion migration on charge carrier injection or extraction at interfaces of this layer with the charge transport layers, included in our model, can also be important.<sup>29</sup> The band alignment of the semiconductor with the electrode work functions is changed by the Debye layers, modifying current injection and electron-hole recombination.<sup>28,30,31</sup>

We have developed a predictive transport model that considers ion motion. This model shows charge build up at the perovskite/charge transport layer interfaces due to ion motion that causes electrostatic potential changes in the perovskite layer and the HTL and ETL, interface recombination, band offsets at the perovskite/charge transport layer interfaces and free charge carrier transport in the HTL and ETL as well as the perovskite layer. A description of the code and a free copy can be downloaded from Ref. 32.

In this article, we use our model, where  $E_A$  is fixed at 0.58 eV, to predict and explain J-V curves at three scan rates and  $H$  and  $J_{sc}$  vs scan rate and temperature. These predictions are validated by comparing with experimental measurements for structure A. Then, we show  $E_A$  can be extracted from measurements of the temperature dependence of  $J_{sc}$  and  $H$  vs scan rate for all four cell structures without the need to model J-V curves for these devices. These  $E_A$  values are compared with our DFT predictions. In addition, we provide predictions from our model for the sensitivity of PCE vs scan rate curves to  $N_0$ , recombination rates and  $E_A$ . Our concluding section summarizes our results and discusses the implications of ion transport for cell stability.

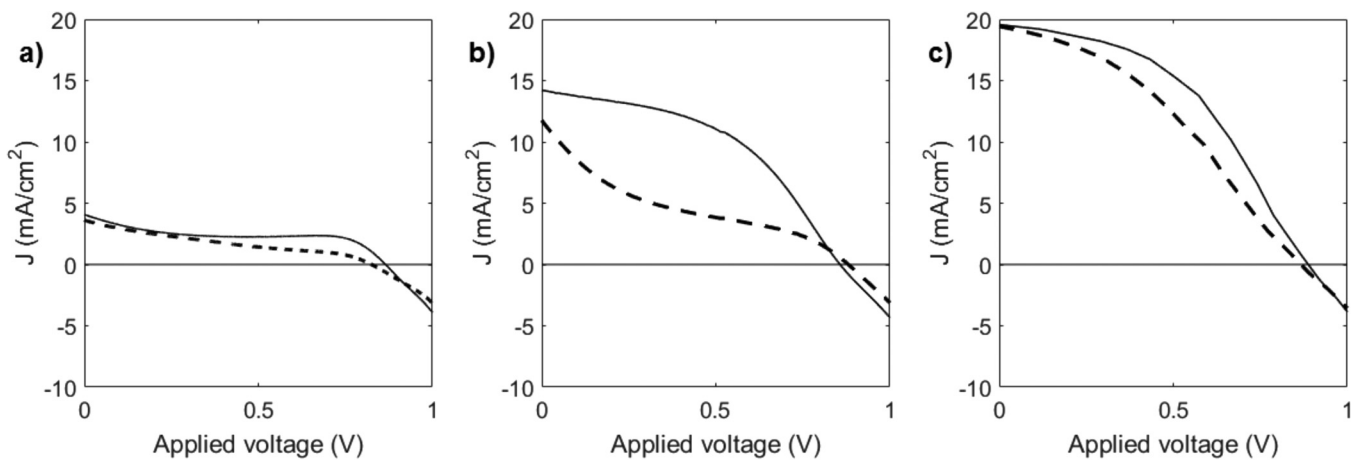


FIG. 2. Experimental J-V curves for structure A illustrating normal hysteresis with scan rates of (a) 1 mV/s, (b) 75 mV/s, and (c) 1 V/s at 315 K. Solid lines indicate the reverse scan and dashed lines the forward scan.

## II. RESULTS AND DISCUSSION

All parameters for the simulation, including the electron and hole recombination velocities at the interfaces between the perovskite layer and charge transport layers, are stated in Table II of the [supplementary material](#), SM, with their sources.

To demonstrate our argument that  $E_A$  can be obtained directly from experiment, the cells we measured were chosen to be those with the most hysteresis (rather than cells with the highest attainable PCEs). In these cells, bulk recombination dominates, so PCEs are

around 12%. These cells were chosen to provide the best possible validation of our approach to determine  $E_A$ . Their low PCEs do not limit the validity of our model, which is applicable to a cell regardless of its PCE, nor do they affect the conclusions drawn here. [Figures 2\(a\)–2\(c\)](#) show measured J–V curves at scan rates (a) slow (1 mV/s), (b) intermediate (75 mV/s), and (c) fast (1 V/s). The applied bias starts at 1.05 V decreasing to 0 V in the reverse scan followed immediately by the forward scan where it is increased to 1.05 V. Predicted J–V curves are shown in [Figs. 3\(a\)–3\(c\)](#) for scan

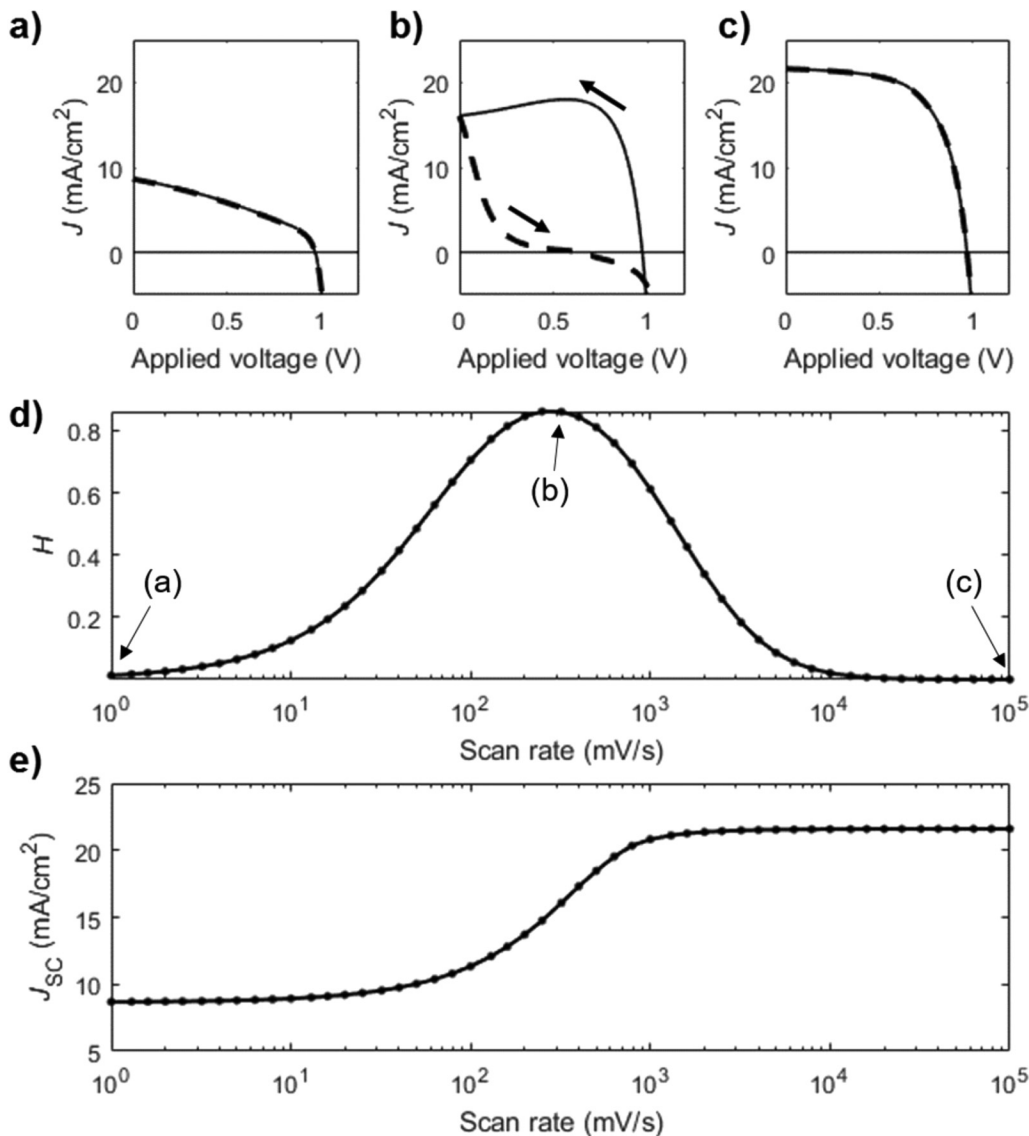


**FIG. 3.** Panels (a)–(c): simulated J–V curves at 315 K for structure A with scan rates indicated by arrows in panel (d): (a) 1 mV/s, (b) 320 mV/s, and (c) 100 V/s. The parameters used for these simulations are given in Table II of the [supplementary material](#) including  $E_A$  set at 0.58 eV for a cubic structure. Solid lines indicate the reverse scan and dashed lines the forward scan. Model predictions for fixed ions are the same as those for the 100 V/s scan in panel (c); without moving ions, there is no dependence on the scan rate and no hysteresis. Panel (d): Hysteresis factor  $H$  as a function of the scan rate. Panel (e): Predicted  $J_{sc}$  as a function of the scan rate.

rates chosen to line up with variations in  $H$ : (a) slow (1 mV/s), (b) intermediate (320 mV/s), and (c) very fast (100 V/s). The simulated characteristic in Fig. 3(b) shows that at intermediate scan rates, the forward scan current density  $J$  drops rapidly. This drop is responsible for the difference in the values of  $J_{sc}$ , of around  $2 \text{ mA/cm}^2$ , observed between the reverse and forward scans in Fig. 2(b). The difference in these values arises because the potentiostat is digitized with a minimum step size of 10 mV, which forces the scan direction to be reversed at  $-8 \text{ mV}$  rather than 0 V. This difference does not affect the conclusions drawn here. Figures 3(d) and 3(e) are plots of  $H$  and  $J_{sc}$ , respectively, vs scan rates from 1 mV/s to 100 V/s. The arrows in Fig. 3(d) show that at scan rates 1 mV/s and 100 V/s,  $H$  and the rate of change of  $J_{sc}$  are close to zero, while at the scan rate (b),  $H$  and the rate of change of  $J_{sc}$  are close to their peak values.

To simulate the J-V curve, the device is initially held at a bias equal to the built-in voltage of 1.05 V, where the internal field is zero for 5 min under illumination. Therefore, vacancies are uniformly distributed at the start of the reverse scan. Figures 2(a) (measurement) and 3(a), 3(d), 3(e) (simulation) demonstrate that little hysteresis is seen at slow scan rates. Here, ion motion is sufficiently fast compared to changes in applied voltage, which the ions keep up with the voltage changes as the applied bias is scanned. The cell behaves as though it were at steady state at the given applied voltage. In this state, the Debye layers at the perovskite/transport layer interfaces screen the electric field from the central region of the perovskite layer, inhibiting migration of electrons and holes to their respective transport layers. Consequently, the bulk recombination rate within the perovskite increased above the level and the current density reduced compared to their values if no mobile ions were present. Discrepancies between Figs. 2(a) and 3(a) may arise from device memory from the previous scans due to very slow-moving ion species<sup>14</sup> and from degradation; a 1 mV/s scan rate, for example, measuring a full scan from 1.2 V requires the device to be continuously operated for around 40 min.

Hysteresis is seen at intermediate scan rates in Figs. 2(b) and 3(b), 3(d), 3(e). As the applied voltage is increased from zero in the forward scan, the current drops steeply initially then flattens out before eventually dropping below zero. Quantitative differences between measured and simulated J-V curves arise from the sensitivity of the simulations to bulk and surface recombination rates. These rates and the relative importance of the bulk compared to surface recombination depend on the processing protocols.<sup>33</sup>

For very fast scans shown in Figs. 2(c) and 3(c), 3(d), 3(e), the ions do not have sufficient time to move and so are effectively fixed in their initial positions. The current is, therefore, independent of the scan direction given that electron and hole motion is always much faster than vacancy motion. This prediction is shown in Video 3 of the supplementary material. Comparing Figs. 2(c) and 3(c), there is qualitative agreement between experiment and simulation, indicating that charge carrier transport is accurately modeled in the absence of hysteresis.

A more detailed understanding of how the interaction between ionic and electronic transport influences device characteristics is obtained from Videos 1–3 of the supplementary material, which show the evolution of the potential profiles when the ion vacancies move toward a new equilibrium following the applied voltage during the scan at the rates used in panels (a)–(c) in Fig. 3,

respectively. Panels in these videos simulated the ion vacancy density, band profiles, the current density, and the bulk electric field over the course of J-V scans. Stills from Video 2 are shown in the supplementary material.

Our predicted potential profiles show qualitative agreement with measured profiles from Kelvin probe force microscopy in Fig. 3 of Ref. 34. We can draw the following conclusions from the videos. First, during a scan, the magnitude and sign of the electric field across the bulk of the perovskite layer are affected by changes in both the applied voltage and the potential drops across each Debye layer. The latter lag *behind* the scan so the internal electric field within the device depends not only on the applied voltage but also on the scanning history. Second, as seen in the stills included in Fig. 1 of the supplementary material, the bulk field changes from positive to negative between reverse and forward scans. When the field is positive, electrons and holes tend to drift toward their respective transport layers, leading to reduced recombination and a higher current density on the reverse scan. Conversely, a negative bulk field by driving carriers in the opposite direction increases recombination near the interfaces and decreases the cell current density. Third, close to the interfaces, there are strong electric fields that enhance the extraction of charge carriers within a few Debye lengths of the interfaces with the transport layers and so reduce interfacial recombination.<sup>10</sup> These fields affect free carrier extraction rates since these rates depend on the difference between the flux leaving the perovskite layer (determined by the gradient of the local charge quasi-Fermi levels) and the surface recombination flux (that varies as the product of the surface recombination velocities and the electron and hole densities at the interface).

Figures 4(a) and 4(b) show simulated  $H$  and  $J_{sc}/J_{scmax}$ , respectively, where  $J_{scmax}$  is the limit as the scan rate tends to infinity, as a function of the scan rate for structure A at temperatures  $T$  from 270 K to 310 K. These curves identify scan rates that measure the speed of the mobile vacancy response. The peak in  $H$  and the onset of current loss are shifted down to the 100 mV/s regime upon cooling. The same effect has been observed in MAPI cells employing organic transport layers.<sup>35,36</sup> For the sigmoidal  $J_{sc}$  vs scan rate curves in Fig. 4(b), we choose the scan rate giving 90%  $J_{scmax}$  since this scan rate lies below the large range of scan rates at which  $J_{sc}$  is close to  $J_{scmax}$ . For  $H$ , we choose the scan rate at which  $H$  obtains its maximum. Figure 4 yields  $E_A$  from these characteristic scan rates plotted vs  $1/(k_B T)$ , from which  $E_A$  is deduced given the Arrhenius temperature dependence of  $D_v$ . Figure 5(a)–5(d) show Arrhenius plots used to extract the values of  $E_A$  from the experiment for each of our four structures shown on the left of each panel. Purple circles indicate the scan rates at which  $J_{sc}$  is 90% of  $J_{scmax}$  (for reasons stated in the discussion on Fig. 4) and green squares the scan rates at which  $H$  reaches its maximum vs  $1/(k_B T)$ . The measurements of  $H$  and  $J_{sc}$  vs scan rate as temperature  $T$  varies from which these plots are taken are shown in Fig. 2 of the supplementary material. For our MAPI and FAPI devices, hysteresis was still measurable at scan rates down to 1 mV/s, making the limit at low scan rates where  $H$  tends to zero hard to ascertain. We suggest the use of settled measurements, for example, holding the device at maximum power point for PCE or holding at open-circuit for  $V_{oc}$  so that the property of interest relaxes to its stable value. Table I compares our  $E_A$  values deduced from measurements

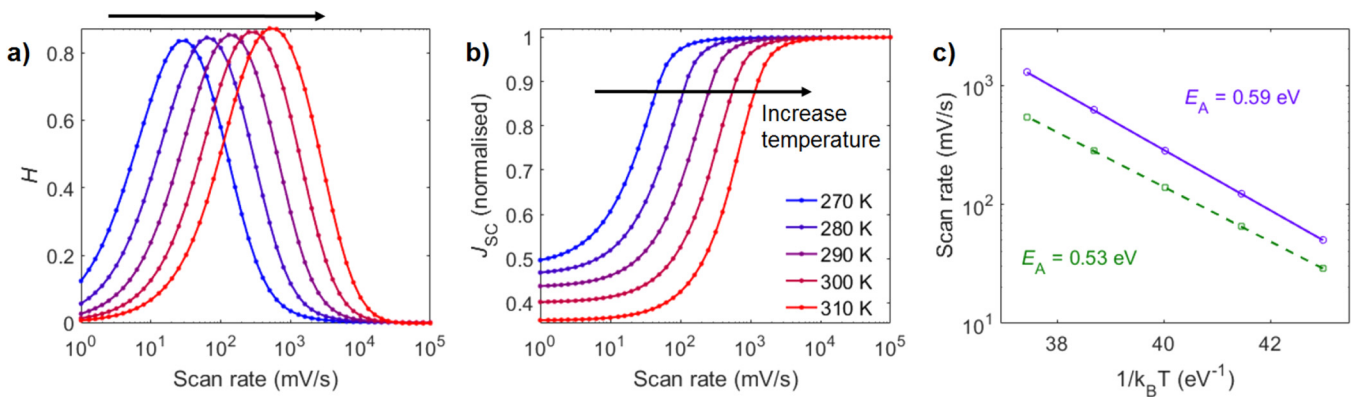


**FIG. 4.** Panel (a) Simulated hysteresis factor  $H$ , panel (b) ratio of the short-circuit current density  $J_{sc}$  to its limiting value  $J_{scmax}$  vs scan rate for structure A. Simulation parameters are shown in Table II of the [supplementary material](#) including  $E_A$  set at 0.58 eV for a cubic structure. The temperature  $T$  runs from 270 K (blue, leftmost curves) to 310 K (red, rightmost curves) in steps of 10 K. Panel (c): The Arrhenius plot of the scan rates at which  $J_{sc}$  is 90% of  $J_{scmax}$  (purple circles, solid lines giving fit to circles, see text for choice of 90%) and where  $H$  is a maximum (green squares, dashed lines giving fit to squares). Temperatures run from 330 K down to 276 K.  $E_A$  is obtained from the gradient of each line and is shown on the plot.

of  $H$  and  $J_{sc}$  vs scan rate as the temperature  $T$  varies for structures A–D and shown in [Fig. 5](#) with predicted  $E_A$  for halide motion for each of the three perovskite materials used in the absorber layers using DFT methods for tetragonal MAPI, FAPI, and MAPBr. For MAPBr, Oranskaia *et al.*<sup>37</sup> predict formation energies of Br vacancies

in MAPBr and FAPBr of 1.25 eV and 1.28 eV, respectively, and  $E_A$  of 0.27 eV and 0.33 eV, respectively. Our values for  $E_A$  deduced from  $J_{sc}$  measurements are within 10% of our DFT prediction of 0.44 eV for tetragonal MAPI and to 0.43 eV deduced from measurements of bulk conductivities.<sup>38</sup>  $E_A$  predicted by first-principles calculations

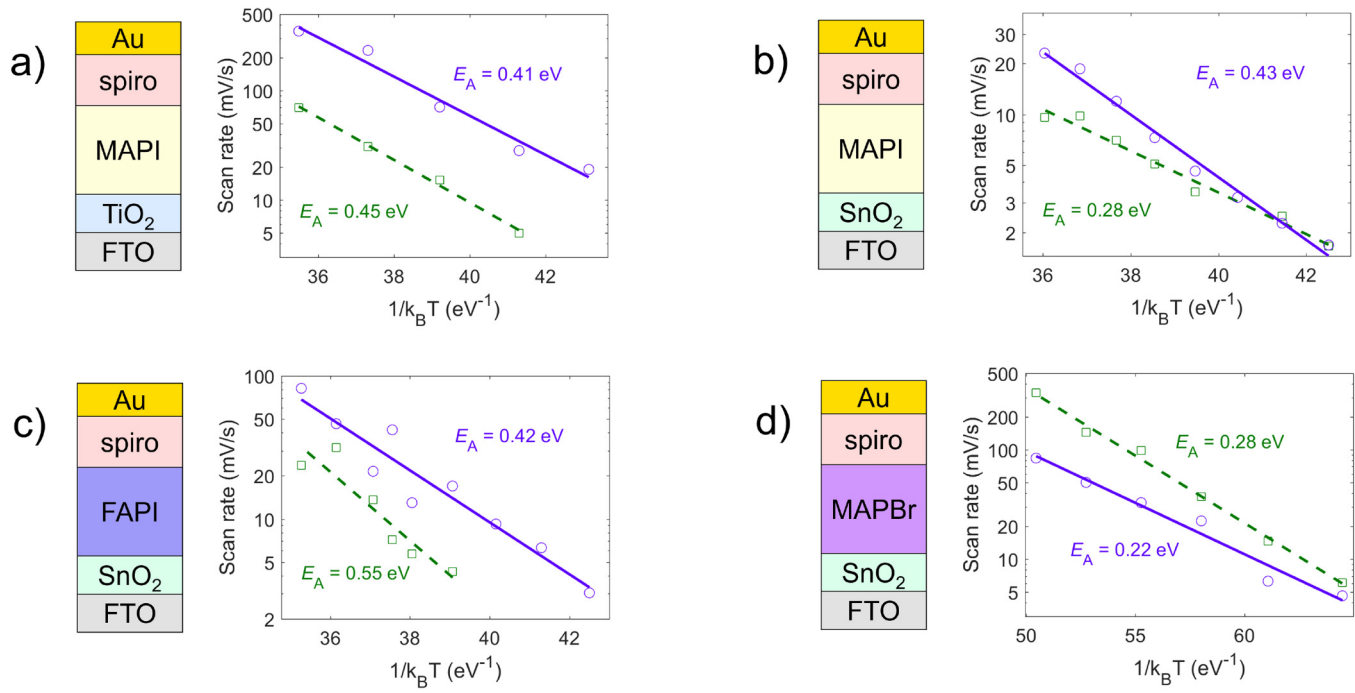


**FIG. 5.** As for [Fig. 4](#) but here each panel shows experimental measurements on each of structures A–D on the left of the panel.  $E_A$  obtained from the gradient of each line is shown on the plot and listed in [Table I](#). Panels (a)–(c) show results at temperatures of 330 K down to 276 K and panel (d) at temperatures of 230 K down to 276 K.

**TABLE I.** Measured activation energies  $E_A$  for each device, using the changes in short-circuit current density  $\Delta J_{sc}$  and hysteresis factor  $\Delta H$  with temperature shown in Fig. 5. The use of a spiro-OMeTAD HTL and a Au back contact was common to all device architectures. DFT values are for tetragonal MAPI, FAPI, and MAPBr.

Perovskite	ETL	$E_A$ ( $\Delta J_{sc}$ ) (eV)	$E_A$ ( $\Delta H$ ) (eV)	$E_A$ (DFT) (eV)
MAPI	TiO <sub>2</sub>	0.41	0.45	0.44
MAPI	SnO <sub>2</sub>	0.43	0.28	0.44
FAPI	SnO <sub>2</sub>	0.42	0.55	0.45
MAPBr	SnO <sub>2</sub>	0.22	0.28	0.36

can vary from 0.06 to 0.65 eV, depending on the MA orientation.<sup>21</sup> For the MAPBr device, structure D, the predicted  $E_A$  from experiment disagrees with the DFT calculations by 0.14 eV. This discrepancy may be linked to the lower temperatures where hysteresis occurs due to the lower  $E_A$  compared to MAPI although the overall trend is correct. From the comparisons with DFT values in Table I, measuring  $J_{sc}$  gives a more reliable measure of  $E_A$  than measuring  $H$ . The maximum in  $H$  vs scan rate depends on the shape of the entire J-V curve, which is sensitive to a wide variety of parameters and interpolating to find the maximum introduces additional errors. In contrast, finding the scan rate at which  $J_{sc}$  is 90% of  $J_{scmax}$  depends on one point on the J-V curve, does not include any effects from the change in the scan direction and is calculated from monotonic plots of  $J_{sc}$  against the scan rate. In Fig. 6, the effects of ionic transport and carrier recombination on the apparent PCE, defined as the maximum value of  $JV$  on the J-V curve obtained by scanning from just above  $V_{oc}$  (i.e., 1.2 V) to  $J_{sc}$  at a fixed scan rate, is shown as a function of the scan rate. Part of the point of this plot is to indicate that there are some quantities, such as defect activation energy  $E_A$ , for which certain changes (e.g., increasing  $E_A$ ) give rise to measurements that may lead to the mistaken impression that they improve stabilized PCE, whereas in fact the results of these changes lead only

to a slowing of the ion dynamics. Nevertheless, changes in other quantities, such as reducing defect density  $N_0$ , can lead to significant improvements in stabilized PCE, but using a dynamic measurement to assess this improvement may still lead to significant errors. In particular, Fig. 6(a) shows the apparent PCE as a function of the scan rate for the simulated device as the defect density is reduced from  $1.6 \times 10^{19} \text{ cm}^{-3}$  by three orders of magnitude. We see that the hysteresis and loss behaviors are shifted to longer timescales and reduced in severity. Our explanation is as follows. As the total number of mobile defects decreases, the potential changes from the Debye regions in the perovskite layers increase at the expense of the potential changes linked to the Debye regions in the transport layers. In addition, the Debye layer widths increase. The ratio of the total potential drop across an interfacial Debye layer in the perovskite to the potential drop in the adjacent transport layer is determined by the dimensionless ratio between the product of permittivity and vacancy density in the perovskite and the product of permittivity and doping density in the adjacent transport layer.<sup>10</sup> For the ETL/perovskite interface, this ratio is denoted by  $\Omega_E^2$ , while for the perovskite/HTL interface, it is denoted by  $\Omega_H^2$ . The effects on cell performance of varying these two ratios by changing the transport layer properties are discussed in Ref. 10. Our model shows a decrease in either the ion vacancy density in the perovskite or the permittivity in the transport layer, and hence  $\Omega_E$  and  $\Omega_H$ , leads to proportionally larger potential drops within the perovskite layer that extend further into the perovskite (Fig. 4 of the [supplementary material](#)). In turn, for lower vacancy densities, the electric fields close to the perovskite/TL interfaces are larger and extend further into the perovskite layer, giving rise to more efficient carrier extraction to the contacts and reduced recombination losses.

Where the vacancy density decreases below  $10^{17} \text{ cm}^{-3}$ , the Debye length becomes so large that the Debye layers extend across the entire cell. As a consequence, the positive electric field on the reverse scan spreads across the entire width of the perovskite layer, even in the slow scan limit, leading to efficient charge separation throughout the perovskite. As shown in Fig. 6(a), the apparent PCE

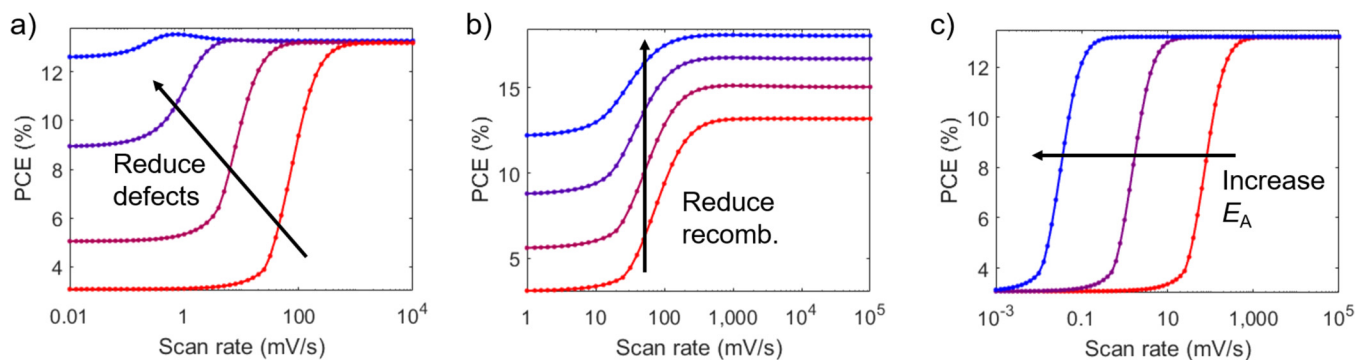


**FIG. 6.** Predicted apparent power conversion efficiency PCE as a function of the scan rate for the device used for Fig. 2. Simulation parameters are shown in Table II of the [supplementary material](#) and the following parameters are varied. Panel (a): The defect density  $N_0$  is reduced from  $1.6 \times 10^{19} \text{ cm}^{-3}$  (red) to  $1.6 \times 10^{16} \text{ cm}^{-3}$  (blue) in decades. Panel (b): All recombination parameters are made less severe from their original values (red) to most favorable (blue). The values of  $\beta$ ,  $v_{nE}$ ,  $v_{pE}$ ,  $v_{nH}$ , and  $v_{pH}$  are taken from the values shown in Table II, divided by 1, 2, 4, and 8. Values of  $\tau_n$  and  $\tau_p$  come from Table II, multiplied by 1, 2, 4, and 8. Panel (c):  $E_A$  for the halide motion is increased from 0.58 (red) to 0.68 and 0.78 eV (blue).

at low defect densities represented by the blue line at all scan rates is close to the apparent PCE for higher defect densities at fast scans during which Debye layers do not have time to form. Larger potential drops within the perovskite as the defect density is reduced lead to vacancies from deeper within the perovskite being drawn into the Debye layers as the charge within these layers evolves. As a consequence, the response time of the ions to a change in applied bias increases, causing an increase in the timescale at which hysteresis is a maximum, which corresponds to the shift to slower scan rates as the vacancy density is reduced as seen in Fig. 6(a).

While the formation of the Debye layers tends to reduce the electric field within the bulk of the absorber, many perovskite devices still show good performance on the forward scan, during which the bulk electric field can be negative, by exhibiting low bulk recombination. Charge carrier diffusion lengths/lifetimes in the perovskite material are often sufficiently long to produce a significant current even where charge extraction takes place via diffusion against an adverse potential gradient. In Fig. 6(b), we show the dependence of performance on the amount of bulk recombination within the perovskite layer and surface recombination at the interfaces for our simulated structure A. Bulk recombination may be increased by recombination at grain boundaries within the perovskite layer as observed in a recent review by Tennyson *et al.*<sup>39</sup> The timescale of the ion motion is unaffected by the level of recombination, and so the scan rate dependence of the behavior displayed in Fig. 6(b) is largely unchanged. The performance improvement as bulk and surface recombination are reduced for all scan rates is shown in Fig. 6(b). The greatest improvement in apparent PCE is for slower scans, where losses due to poor charge separation are the largest. Figure 3 of the [Supplementary material](#) explores the variation of the four standard metrics of performance ( $J_{sc}$ ,  $V_{oc}$ , PCE, and FF) with the recombination multiplier defined in the caption for Fig. 6.

In Fig. 6(c), we show the effect of increasing  $E_A$  from 0.58 eV<sup>22</sup> to 0.68 and 0.78 eV. Debye layers still form, regardless of the value of  $E_A$ , albeit more slowly as  $E_A$  increases, and so there is no resulting increase in the settled PCE, given by the apparent PCE at slow scan rates in Fig. 6(c).

### III. CONCLUSIONS

We have investigated transient behavior exhibited by perovskite solar cells (PSCs) with a mix of experiment and theory. From a drift-diffusion model that accounts for both ion vacancy and charge carrier transport, we can reproduce the observed behavior of PSCs during J-V scans, including the dependence of the J-V curve on the scan rate and temperature. Videos in the [supplementary material](#) show the cell response throughout a J-V scan. In line with previous results,<sup>25,40–43</sup> we find that hysteresis in the J-V curves of PSCs is primarily caused by the flow of halide ions in and out of narrow Debye layers at the edges of the perovskite film which screen the electric field.

Furthermore, we show that the extent to which hysteresis is present depends on the alignment of the timescales of the scan and ion motion within the film. In the devices we considered, the screening of the electric field from the perovskite layer significantly reduces device performance by hindering charge separation in the perovskite,

even where hysteresis is not observed. However, for cells fabricated with sufficiently long charge carrier diffusion lengths, where charge separation is not such a major issue, this need not be the case. Moreover, we were able to confirm predictions from the model by comparing to experimental data from the four different PSCs.

If hysteresis is not present when a device is measured, we suggest investigating other scan rates and temperatures to find the slow scan limit. For our MAPI and FAPI devices, hysteresis was still present even for scan rates down to 1 mV/s. To remedy this problem, we suggest the use of settled measurements, for example, holding the device at maximum power point for PCE or holding at open-circuit for  $V_{oc}$  so that the property of interest relaxes to its stable value.

Our model is predictive in that we have shown how the short-circuit current density and hysteresis factor can be used to predict the activation energy of ion motion  $E_A$ . We have used these predictions to establish an experimental technique for extracting the activation energies of the ion diffusion in real devices. This technique requires measurements of the temperature variation of (i) the scan rate corresponding to maximum hysteresis and (ii) the scan rate at which  $J_{sc}$  reaches 90% of its maximum value. The results we obtained from these two sets of measurements are in broad agreement with each other and with DFT calculations and other experimental values.

We find that reductions in ion vacancy density reduce recombination and improve settled PCE for cells limited by recombination in the bulk of the perovskite. In contrast, we found slowing down of the diffusion of ion vacancies by increasing the activation energy shifts losses to longer timescales but does not mitigate efficiency loss at a steady state.

A device appearing to be hysteresis-free may be scanned at a rate or a temperature at which hysteresis is negligible. Measurable levels of hysteresis have been seen when the temperature is changed. For example, a MAPI cell with organic transport layers that was hysteresis-free at room temperature and standard scan rates exhibited severe hysteresis upon cooling to 175 K.<sup>35</sup>

Our model shows that hysteresis can be reduced by lowering  $N_0$  and recombination rates. This result explains why the following approaches have been found to achieve these goals: (i) widespread adoption of mixed cation perovskites;<sup>44–46</sup> (ii) surface passivation, which reduces surface vacancy densities;<sup>47</sup> and (iii) the minimization of the compressive lattice strain to reduce the equilibrium halide vacancy density correlates with strain and that strained regions show increased non-radiative recombination.<sup>48</sup>

The strain caused by the ion transport occurs in the regions of significant buildup and depletion of the ion vacancy density at the edges of the perovskite. Ion buildup/depletion has also been found to lead to carrier buildup,<sup>25,42,43,49</sup> which, in turn, contributes to additional Ohmic heating and thermal breakdown.<sup>50</sup> This heating may cause problems if the temperature within the perovskite passes through a phase transition, for example, the transition in MAPI around 327 K from tetragonal to cubic.<sup>51</sup> Another degradation pathway in perovskites has been linked to the highly reactive  $O_2^-$  superoxide species that is generated from the reaction of free electrons in the perovskite with molecular oxygen. *Ab initio* simulations indicate that iodide vacancies are the preferred site for  $O_2^-$  formation.<sup>52</sup> Therefore, reducing the ion vacancy density is likely to benefit not just cell performance but also the long-term stability of PSCs.

## IV. METHODS

### A. Modeling

A description of the DFT based calculations for the  $E_A$  values is given in Sec. 2 of the [supplementary material](#).

Our drift-diffusion (DD) picture is described by Courtier *et al.*<sup>10</sup> We model the motion of electrons, holes, and halide ion vacancies within a planar PSC. The perovskite absorber and both transport layers (TLs) are all explicitly modeled. A similar model has been employed by others<sup>53,54</sup> to study impedance and transient current measurements. Our model goes beyond earlier work by ourselves<sup>25</sup> and others<sup>41</sup> by explicitly including the TLs, allowing for conduction and valence band offsets at the ETL/perovskite and perovskite/HTL interfaces. Inclusion of the TLs is crucial for accurate simulation of recombination at the TL/perovskite interfaces. We go beyond<sup>25,55</sup> in including the influence of carriers on the potential and beyond<sup>56</sup> by allowing the distribution of ions to vary during J-V scans. The assumed value of the ion diffusion coefficient in Ref. 40 is  $10^6$  times greater than that of Ref. 22, and voltage scan rates are around  $10^6$  times greater than the experimental scan rates at which hysteresis is observed. In Ref. 57, the modeled ion concentration profile is fixed to its equilibrium profile.

In some descriptions of the ion motion, positive and negative species are assumed to have similar mobilities,<sup>12</sup> causing a spatially symmetric distribution of charge with respect to an axis midway across the perovskite layer. We argue that this description is incorrect. The migration of iodide anions via lattice interstitials will not contribute appreciably to the overall ion transport. In Minns *et al.*,<sup>58</sup> no measurement of the ion diffusion coefficient is reported and the concentration of interstitial species is low. MA<sup>+</sup> cations have also been suggested to contribute to ion conduction but their small diffusion coefficient rules out a significant contribution at the same timescales as that of the halide vacancies.<sup>59</sup> Wu *et al.*<sup>12</sup> employed this model to study steady-state characteristics, but we would note that such a model is only valid for times much longer than the time for ion vacancies to migrate across the perovskite layer and at these long timescales, we found experimental evidence of degradation.

We numerically integrate the full drift-diffusion equations using a scheme based on the work of Courtier *et al.*<sup>43</sup> that has been used to validate simulations with one-dimensional solver using the Quokka3 software.<sup>60</sup> The scheme of Courtier *et al.* makes use of a non-uniform spatial discretization that clusters points around the ETL/perovskite and perovskite/HTL interfaces, where the presence of Debye layers gives rise to extremely rapidly varying solutions. A detailed description of the model, and its numerical solution, is given in Sec. 3 of the [supplementary material](#). In particular, the full set of equations is given in (S1)–(S15) with boundary conditions in (16)–(31). Table I of the [supplementary material](#) defines the symbols. The applied voltage and the built-in field are included via appropriate boundary conditions on Poisson's equation. The time variation of the applied voltage is accomplished by making the boundary conditions a function of time.

Electrons and holes are generated and can recombine in the perovskite. Electrons exist only in the perovskite and ETL, while holes exist only in the perovskite and HTL due to the large energy barriers (more than an eV) that prevent each type of carrier from entering the opposite TL. The ratio of the carrier density on the higher-energy

side of a potential barrier  $\Delta E$  compared to on the lower-energy side is given by the Boltzmann statistics to be  $\exp -\Delta E/k_B T$ . For a modest barrier of 1 eV at room temperature, this factor gives a reduction in the density of around 17 orders of magnitude.

### B. Experiment

The materials used, their sources, and device fabrication are stated in Sec. 1 of the [supplementary material](#). The J-V response of the perovskite devices was recorded as a function of sweep rate (1000 to 1 mV/s in logarithmic steps with  $\Delta V = 10$  mV) with Metrohm Autolabs PGSTAT12 potentiostat. Devices were pre-conditioned under illumination at +1.2 V (or +1.6 V for MAPBr) forward bias for 5 min before each scan. Reverse scans (forward bias to short circuit) were recorded before immediately switching into forward scans (short circuit to forward bias). After each scan, the device would again equilibrate for 5 min under forward bias before moving onto the next sweep rate.

Illumination was not interrupted until after the completion of the J-V regimen. Temperature and illumination control were implemented by a Linkam LTS-420-E cryostat connected to a PAIOS 2.0 characterization system (Fluxim, Switzerland). The cryo-stage was purged with a protective layer of dry nitrogen before use. Sample temperature was recorded with a PT100 resistance temperature detector in the thermal contact with the solar cell. Illumination came from a white LED coupled into the cryostat with a light tube. The cell PCEs were evaluated from J-V characteristics obtained at a scan rate of 1 mV/s at 1 sun illumination.

## SUPPLEMENTARY MATERIAL

See the [supplementary material](#) for materials synthesis and device fabrication (Sec. I A), DFT simulation (Sec. I B), and the drift diffusion model (Sec. I C). The supplementary material also includes Figs. 1–4 and Videos 1–3. Videos 1–3 are for scan rates of 1 mV/s, 320 mV/s, 100 V/s respectively.

## AUTHORS' CONTRIBUTIONS

J.M.C., A.B.W., G.R., and M.S.I. wrote the manuscript. J.M.C. ran the simulations. J.M.C., I.A.B., A.A.D., and T.W.J. made experimental measurements. D.G. carried out DFT simulations. J.M.C., N.E.C., and J.M.F. developed and coded the DD numerical scheme. J.M.C., N.E.C., K.F., G.R., and A.B.W. contributed to interpreting the DD model. J.M.F. and G.R. conceived and formulated the DD model. T.W.J., K.F.A., and L.L. fabricated the devices. K.F., J.M.F., G.R., M.S.I., and A.B.W. supervised the theoretical work. T.W.J. and G.J.W. supervised the experimental work. All authors contributed to revising of the manuscript.

## ACKNOWLEDGMENTS

We would like to thank Chris Fell and Laurie Peter for their careful reading of the manuscript. J.M.C. and N.E.C. acknowledge EPSRC funded studentships from the CDT in New and Sustainable Photovoltaics (No. EP/L01551X/1). This work has received funding from the Australian Renewable Energy Agency (ARENA) as part of ARENA's Emerging Renewables Program via Grant No. P159394. D.G., A.B.W., and S.I. received funding from the European Union's

Horizon 2020 research and innovation programme under EoCoE (Grant Agreement No. 676629) and A.B.W. under EoCoE II (Grant Agreement No. 824158).

## DATA AVAILABILITY

The data that support the findings of this study are available within the article (and its [supplementary material](#)).

## REFERENCES

- <sup>1</sup>A. Extance, "The reality behind solar power's next star material," *Nature* **570**, 429 (2019).
- <sup>2</sup>D. P. Buemi, "Perovskite solar cells: Hero, villain or just plain fantasy?," *Solar Power World* (2020).
- <sup>3</sup>M. S. Islam, "Ionic transport in  $\text{ABO}_3$  perovskite oxides: A computer modelling tour," *J. Mater. Chem.* **10**, 1027–1038 (2000).
- <sup>4</sup>W. A. Dunlap-Shohl, Y. Zhou, N. P. Padture, and D. B. Mitzi, "Synthetic approaches for halide perovskite thin films," *Chem. Rev.* **119**, 3193–3295 (2019).
- <sup>5</sup>S. D. Stranks and H. J. Snaith, "Metal-halide perovskites for photovoltaic and light-emitting devices," *Nat. Nanotech.* **10**, 391–402 (2015).
- <sup>6</sup>C. Li, S. Tscheuschner, F. Paulus, P. E. Hopkinson, J. Kießling, A. Köhler, Y. Vaynzof, and S. Huettnner, "Iodine migration and its effect on hysteresis in perovskite solar cells," *Adv. Mater.* **28**, 2446–2454 (2016).
- <sup>7</sup>A. Bercegol, S. Cacovich, G. Vidon, S. Mejaouri, A. Yaiche, J.-B. Puel, C. Longeaud, J.-F. Guillemoles, S. Jutteau, J. Rousset, D. Ory, and L. Lombez, "Imaging electron, hole, and ion transport in halide perovskite," *J. Phys. Chem. C* **124**, 11741–11748 (2020).
- <sup>8</sup>W. Yu, F. Li, L. Yu, M. R. Niazi, Y. Zou, D. Corzo, A. Basu, C. Ma, S. Dey, M. L. Tietze, U. Buttner, X. Wang, Z. Wang, M. N. Hedhili, C. Guo, T. Wu, and A. Amassian, "Native defect-induced hysteresis behavior in organolead iodide perovskite solar cells," *Nat. Commun.* **9**, 5354 (2018).
- <sup>9</sup>B. Hwang and J.-S. Lee, "Hybrid organic-inorganic perovskite memory with long-term stability in air," *Sci. Rep.* **7**, 673 (2017).
- <sup>10</sup>N. E. Courtier, J. M. Cave, J. M. Foster, A. B. Walker, and G. Richardson, "How transport layer properties affect perovskite solar cell performance: Insights from a coupled charge transport/ion migration model," *Energy Environ. Sci.* **12**, 396–409 (2019).
- <sup>11</sup>M. V. Khenkin, E. A. Katz, A. Abate, G. Bardizza, and J. J. E. A. Berry, "Consensus statement for stability assessment and reporting for perovskite photovoltaics based on ISOS procedures," *Nat. Energy* **5**, 35–49 (2020).
- <sup>12</sup>N. Wu, D. Walter, A. Fell, Y. Wu, and K. Weber, "The impact of mobile ions on the steady-state performance of perovskite solar cells," *J. Phys. Chem. C* **124**, 219–229 (2020).
- <sup>13</sup>C.-J. Tong, L. Li, L.-M. Liu, and O. V. Prezhdo, "Synergy between ion migration and charge carrier recombination in metal-halide perovskites," *J. Am. Chem. Soc.* **142**, 3060–3068 (2020).
- <sup>14</sup>K. Domanski, B. Roose, T. Matsui, M. Saliba, S.-H. Turren-Cruz, J.-P. Correa-Baena, C. R. Carmona, G. Richardson, J. M. Foster, F. De Angelis, J. M. Ball, A. Petrozza, N. Mine, M. K. Nazeeruddin, W. Tress, M. Grätzel, U. Steiner, A. Hagfeldt, and A. Abate, "Migration of cations induces reversible performance losses over day/night cycling in perovskite solar cells," *Energy Environ. Sci.* **10**, 604–613 (2017).
- <sup>15</sup>G. A. Nemnes, C. Besleaga, V. Stancu, D. E. Dogaru, L. N. Leonat, L. Pintilie, K. Torfason, M. Ilkov, A. Manolescu, and I. Pintilie, "Normal and inverted hysteresis in perovskite solar cells," *J. Phys. Chem. C* **121**, 11207–11214 (2017).
- <sup>16</sup>G. A. Nemnes, C. Besleaga, A. G. Tomulescu, A. Palici, L. Pintilie, A. Manolescu, and I. Pintilie, "How measurement protocols influence the dynamic J-V characteristics of perovskite solar cells: Theory and experiment," *Sol. Energy* **173**, 976–983 (2018).
- <sup>17</sup>Y. Hou, S. Scheiner, X. Tang, N. Gasparini, M. Richter, N. Li, P. Schweizer, S. Chen, H. Chen, C. O. R. Quiroz, X. Du, G. J. Matt, A. Osvet, E. Spiecker, R. H. Fink, A. Hirsch, M. Halik, and C. J. Brabec, "Suppression of hysteresis effects in organohalide perovskite solar cells," *Adv. Mater. Interfaces* **4**, 1700007 (2017).
- <sup>18</sup>H. J. Snaith, A. Abate, J. M. Ball, G. E. Eperon, T. Leijtens, N. K. Noel, S. D. Stranks, J. T.-W. Wang, K. Wojciechowski, and W. Zhang, "Anomalous hysteresis in perovskite solar cells," *J. Phys. Chem. Lett.* **5**, 1511–1515 (2014).
- <sup>19</sup>S. N. Habisreutinger, N. K. Noel, and H. J. Snaith, "Hysteresis index: A figure without merit for quantifying hysteresis in perovskite solar cells," *ACS Energy Lett.* **118**, 2472–2476 (2018).
- <sup>20</sup>A. Walsh, D. O. Scanlon, S. Chen, X. G. Gong, and S.-H. Wei, "Self-regulation mechanism for charged point defects in hybrid halide perovskites," *Angew. Chem. Int. Ed.* **127**, 1811 (2015).
- <sup>21</sup>C.-J. Tong, W. Geng, O. V. Prezhdo, and L.-M. Liu, "Role of methylammonium orientation in ion diffusion and current-voltage hysteresis in the  $\text{CH}_3\text{NH}_3\text{PbI}_3$  perovskite," *ACS Energy Lett.* **2**, 1997–2004 (2017).
- <sup>22</sup>C. Eames, J. M. Frost, P. R. F. Barnes, B. C. O'Regan, A. Walsh, and M. S. Islam, "Ionic transport in hybrid lead iodide perovskite solar cells," *Nat. Commun.* **6**, 7497 (2015).
- <sup>23</sup>A. Walsh and S. D. Stranks, "Taking control of ion transport in halide perovskite solar cells," *ACS Energy Lett.* **3**, 1983–1990 (2018).
- <sup>24</sup>S. Reichert, Q. An, Y.-W. Woo, A. Walsh, Y. Vaynzof, and D. Carsten, "Probing the ionic defect landscape in halide perovskite solar cells," *arXiv:2005.06942* (2020).
- <sup>25</sup>G. Richardson, S. E. J. O'Kane, R. G. Niemann, T. A. Peltola, J. M. Foster, P. J. Cameron, and A. B. Walker, "Can slow-moving ions explain hysteresis in the current-voltage curves of perovskite solar cells?," *Energy Environ. Sci.* **9**, 1476–1485 (2016).
- <sup>26</sup>R. A. Kerner and B. P. Rand, "Ionic-electronic ambipolar transport in metal halide perovskites: Can electronic conductivity limit ionic diffusion?," *J. Phys. Chem. Lett.* **9**, 132–137 (2018).
- <sup>27</sup>J. Mizusaki, K. Arai, and K. Fukui, "Ionic conduction of the perovskite-type halides," *Solid State Ion.* **11**, 203–211 (1983).
- <sup>28</sup>A. Pockett, G. E. Eperon, N. Sakai, H. J. Snaith, L. M. Peter, and P. J. Cameron, "Microseconds, milliseconds and seconds: Deconvoluting the dynamic behaviour of planar perovskite solar cells," *Phys. Chem. Chem. Phys.* **19**, 5959–5970 (2017).
- <sup>29</sup>A. Rizzo, F. Lamberti, M. Buonomo, N. Wrachien, L. Torto, N. Lago, S. Sansoni, R. Pilot, M. Prato, N. Michieli, M. Meneghetti, G. Meneghesso, and A. Cester, "Understanding lead iodide perovskite hysteresis and degradation causes by extensive electrical characterization," *Sol. Energy Mater. Sol. Cells* **189**, 43–52 (2019).
- <sup>30</sup>S. Meloni, T. Moehl, W. Tress, M. Franckevičius, M. Saliba, Y. H. Lee, P. Gao, M. K. Nazeeruddin, S. M. Zakeeruddin, U. Rothlisberger, and M. Grätzel, "Ionic polarization-induced current-voltage hysteresis in  $\text{CH}_3\text{NH}_3\text{PbX}_3$  perovskite solar cells," *Nat. Commun.* **7**, 10334 (2016).
- <sup>31</sup>O. Almora, I. Zarazua, I. Mas-Marza, E. Mora-Sero, J. Bisquert, and G. Garcia-Belmonte, "Capacitive dark currents, hysteresis, and electrode polarization in lead halide perovskite solar cells," *J. Phys. Chem. Lett.* **6**, 1645–1652 (2015).
- <sup>32</sup>N. E. Courtier, J. M. Cave, S. E. J. O'Kane, A. B. Walker, G. Richardson, and J. M. Foster, "IonMonger: A free and fast planar perovskite solar cell simulator with coupled ion vacancy and charge carrier dynamics," *J. Comput. Electron.* **18**, 1435–1449 (2019).
- <sup>33</sup>L. M. Herz, "Charge-carrier dynamics in organic-inorganic metal halide perovskites," *Annu. Rev. Phys. Chem.* **67**, 65–89 (2016).
- <sup>34</sup>S. Weber, I. M. Hermes, S. H. Turren Cruz, C. Gort, V. W. Bergmann, L. Gilson, A. Hagfeldt, M. Grätzel, W. Tress, and R. Berger, "How the formation of interfacial charge causes hysteresis in perovskite solar cells," *Energy Environ. Sci.* **11**2404–2414 (2018).
- <sup>35</sup>D. Bryant, S. Wheeler, B. C. O'Regan, T. Watson, P. R. F. Barnes, D. Worsley, and J. Durrant, "Observable hysteresis at low temperature in 'hysteresis free' organic-inorganic lead halide perovskite solar cells," *J. Phys. Chem. Lett.* **6**, 3190–3194 (2015).
- <sup>36</sup>I. Levine, P. K. Nayak, J. T.-W. Wang, N. Sakai, S. Van Reenen, T. M. Brenner, S. Mukhopadhyay, H. J. Snaith, G. Hodes, and D. Cahen, "Interface-dependent

- ion migration/accumulation controls hysteresis in  $\text{MAPbI}_3$  solar cells," *J. Phys. Chem. C* **120**, 16399–16411 (2016).
- <sup>37</sup>A. Oranskaia, J. Yin, O. M. Bakr, J.-L. Brédas, and O. F. Mohammed, "Halogen migration in hybrid perovskites: The organic cation matters," *J. Phys. Chem. Lett.* **9**, 5474 (2018).
- <sup>38</sup>T.-Y. Yang, G. Gregori, N. Pellet, M. Grätzel, and J. Maier, "The significance of ion conduction in a hybrid organic-inorganic lead-iodide-based perovskite photosensitizer," *Angew. Chem. Int. Ed.* **54**, 7905 (2015).
- <sup>39</sup>E. M. Tennyson, T. A. S. Doherty, and S. D. Stranks, "Heterogeneity at multiple length scales in halide perovskite semiconductors," *Nat. Rev. Mater.* **4**, 573–587 (2019).
- <sup>40</sup>S. van Reenen, M. Kemerink, and H. J. Snaith, "Modeling anomalous hysteresis in perovskite solar cells," *J. Phys. Chem. Lett.* **6**, 3808–3814 (2015).
- <sup>41</sup>D. Moia, I. Gelmetti, P. Calado, W. Fisher, M. Stringer, O. Game, Y. Hu, P. Docampo, D. Lidzey, E. Palomares, J. Nelson, and P. R. F. Barnes, "Ionic-to-electronic current amplification in hybrid perovskite solar cells: Ionically gated transistor-interface circuit model explains hysteresis and impedance of mixed conducting devices," *Energy Environ. Sci.* **12**, 1296–1308 (2019).
- <sup>42</sup>S. E. J. O'Kane, G. Richardson, A. Pockett, R. G. Niemann, J. M. Cave, N. Sakai, G. E. Eperon, H. J. Snaith, J. M. Foster, P. J. Cameron, and A. B. Walker, "Measurement and modelling of dark current decay transients in perovskite solar cells," *J. Mater. Chem. C* **5**, 452–462 (2017).
- <sup>43</sup>N. E. Courtier, G. Richardson, and J. M. Foster, "A fast and robust numerical scheme for solving models of charge carrier transport and ion vacancy motion in perovskite solar cells," *Appl. Math. Model.* **63**, 329–348 (2018).
- <sup>44</sup>D. Ghosh, P. Walsh Atkins, M. S. Islam, A. B. Walker, and C. Eames, "Good vibrations: Locking of octahedral tilting in mixed-cation iodide perovskites for solar cells," *ACS Energy Lett.* **2**, 2424–2429 (2017).
- <sup>45</sup>B. Charles, J. Dillon, O. J. Weber, M. S. Islam, and M. T. Weller, "Understanding the stability of mixed A-cation lead iodide perovskites," *J. Mater. Chem. A* **5**, 22495–22499 (2017).
- <sup>46</sup>M. Saliba, T. Matsui, J.-Y. Seo, K. Domanski, J.-P. Correa-Baena, M. K. Nazeeruddin, S. M. Zakeeruddin, W. Tress, A. Abate, A. Hagfeldt, and M. Grätzel, "Cesium-containing triple cation perovskite solar cells: Improved stability, reproducibility and high efficiency," *Energy Environ. Sci.* **9**, 1989–1997 (2016).
- <sup>47</sup>S. P. Senanayak, B. Yang, T. H. Thomas, N. Giesbrecht, W. Huang, E. Gann, B. Nair, K. Goedel, S. Guha, X. Moya, C. R. McNeill, P. Docampo, A. Sadhanala, R. H. Friend, and H. Sirringhaus, "Understanding charge transport in lead iodide perovskite thin-film field-effect transistors," *Sci. Adv.* **3**, e1601935 (2017).
- <sup>48</sup>T. W. Jones, A. Osharov, M. Alsari, M. Sponseller, B. C. Duck, Y.-K. Jung, C. Settens, F. Nirouzi, R. Brenes, C. V. Stan, Y. Li, M. Abdi-Jalebi, N. Tamura, J. E. Macdonald, M. Burghammer, R. H. Friend, V. Bulović, A. Walsh, G. J. Wilson, S. Lilliu, and S. D. Stranks, "Lattice strain causes non-radiative losses in halide perovskites," *Energy Environ. Sci.* **12**, 596–606 (2019).
- <sup>49</sup>P. Calado, A. M. Telford, D. Bryant, X. Li, J. Nelson, B. C. O'Regan, and P. R. Barnes, "Evidence for ion migration in hybrid perovskite solar cells with minimal hysteresis," *Nat. Commun.* **7**, 995 (2016).
- <sup>50</sup>J. O'Dwyer, *The Theory of Electrical Conduction and Breakdown in Solid Dielectrics* (Clarendon Press, Oxford, 1973).
- <sup>51</sup>D. W. Miller, G. E. Eperon, E. T. Roe, C. W. Warren, H. J. Snaith, and M. C. Lonergan, "Defect states in perovskite solar cells associated with hysteresis and performance," *Appl. Phys. Lett.* **109**, 153902 (2016).
- <sup>52</sup>N. Aristidou, C. Eames, I. Sanchez-Molina, X. Bu, J. Kosco, M. Islam, and S. Haque, "Fast oxygen diffusion and iodide defects mediate oxygen-induced degradation of perovskite solar cells," *Nat. Commun.* **8**, 15215 (2017).
- <sup>53</sup>D. A. Jacobs, H. Shen, F. Pfeffer, J. Peng, T. P. White, F. J. Beck, and K. R. Catchpole, "The two faces of capacitance: New interpretations for electrical impedance measurements of perovskite solar cells and their relation to hysteresis," *J. Appl. Phys.* **124**, 225702 (2018).
- <sup>54</sup>M. Neukom, A. Schiller, S. Zülfie, E. Knapp, J. Ávila, D. Pérez-del Rey, C. Dreesen, K. P. Zanoni, M. Sessolo, H. J. Bolink, and B. Ruhstaller, "Consistent device simulation model describing perovskite solar cells in steady-state, transient, and frequency domain," *ACS Appl. Mater. Interfaces* **11**, 23320–23328 (2019).
- <sup>55</sup>T.-Y. Zhu and D.-J. Shu, "Role of ionic charge accumulation in perovskite solar cell: Carrier transfer in bulk and extraction at interface," *J. Phys. Chem. C* **123**, 5312–5320 (2019).
- <sup>56</sup>D. A. Jacobs, Y. Wu, H. Shen, C. Barugkin, F. J. Beck, T. P. White, K. Weber, and K. R. Catchpole, "Hysteresis phenomena in perovskite solar cells: The many and varied effects of ionic accumulation," *Phys. Chem. Chem. Phys.* **19**, 3094–3103 (2017).
- <sup>57</sup>L. Bertoluzzi, R. A. Belisle, K. A. Bush, R. Cheacharoen, M. D. McGehee, and B. C. O'Regan, "In situ measurement of electric-field screening in hysteresis-free  $\text{PTAA}/\text{FA}_{0.83}\text{Cs}_{0.17}\text{Pb}(\text{I}_{0.83}\text{Br}_{0.17})_3/\text{C}_{60}$  perovskite solar cells gives an ion mobility of  $3 \times 10^{-7} \text{ cm}^2/(\text{Vs})$ , 2 orders of magnitude faster than reported for metal-oxide-contacted perovskite cells with hysteresis," *J. Am. Chem. Soc.* **140**, 12775–12784 (2018).
- <sup>58</sup>J. L. Minns, P. Zajdel, D. Chernyshov, W. van Beek, and M. A. Green, "Structure and interstitial iodide migration in hybrid perovskite methylammonium lead iodide," *Nat. Commun.* **8**, 15152EP (2017).
- <sup>59</sup>A. Senocrate, I. Moudrakovski, G. Y. Kim, T.-Y. Yang, G. Gregori, M. Grätzel, and J. Maier, "The nature of ion conduction in methylammonium lead iodide: A multimethod approach," *Angew. Chem. Int. Ed.* **56**, 7755–7759 (2017).
- <sup>60</sup>D. Walter, A. Fell, Y. Wu, T. Duong, C. Barugkin, N. Wu, T. White, and K. Weber, "Transient photovoltage in perovskite solar cells: Interaction of trap-mediated recombination and migration of multiple ionic species," *J. Phys. Chem. C* **122**, 11270–11281 (2018).

# Supplementary Material: Deducing transport properties of mobile vacancies from perovskite solar cell characteristics

James M. Cave,<sup>1</sup> Nicola E. Courtier,<sup>2</sup> Isabelle A. Blakborn,<sup>3</sup> Timothy W. Jones,<sup>3</sup> Dibyajyoti Ghosh,<sup>4</sup> Kenrick F. Anderson,<sup>3</sup> Liangyou Lin,<sup>3</sup> Andrew A. Dijkhoff,<sup>3</sup> Gregory J. Wilson,<sup>3</sup> Krishna Feron,<sup>3</sup> M. Saiful Islam,<sup>5</sup> Jamie M. Foster,<sup>6</sup> Giles Richardson,<sup>2</sup> and Alison B. Walker<sup>1</sup>

<sup>1)</sup>Department of Physics, University of Bath, BA2 7AY, UK

<sup>2)</sup>Mathematical Sciences, University of Southampton, SO17 1BJ, UK

<sup>3)</sup>CSIRO Energy, Newcastle Energy Centre, 10 Murray Dwyer Circuit, Mayfield West, NSW 2304, Australia<sup>a)</sup>

<sup>4)</sup>Department of Physics, University of Bath, BA2 7AY, UK<sup>b)</sup>

<sup>5)</sup>Department of Chemistry, University of Bath, BA2 7AY, UK

<sup>6)</sup>Department of Mathematics, University of Portsmouth, PO1 3HF, UK

(Dated: 13 October 2020)

## I. METHODS

### A. Materials Synthesis and Device Fabrication

F-doped tin oxide (FTO, 8 Ω/sq) was sourced from Pilkington, USA. Organic perovskite salts were purchased from Dyesol, Australia. Lead halide salts were purchased from TCI, Japan. Milli-Q water was freshly prepared to >18.2 MΩ cm. N,N-dimethylformamide (DMF, 99.8%), dimethylsulfoxide (DMSO, 99.8%), absolute ethanol (200 Proof), isopropanol (99.8%), chlorobenzene (99.8%), acetonitrile (99.8%), were sourced from Sigma-Aldrich and kept under N<sub>2</sub> for use. SnCl<sub>4</sub>·5H<sub>2</sub>O (98%), SnCl<sub>2</sub>·2H<sub>2</sub>O (≥99.99%), 3-mercaptopropionic acid (>99%), hydrochloric acid (37 wt.%), titanium(IV) tetraisopropoxide (>97%), urea (99–101%), lithium trifluorosulfonimide (LiTFSI; 99.85%) were sourced from Sigma-Aldrich and used as received. Hole transport material spiro-OMeTAD (>99%) was purchased from Lumtec and used as received. Metallic Au (>99.9%) was purchased from John Lazos and Associates.

FTO substrates were isolated by laser ablation before cleaning in successive 30 min ultrasonic treatments in 2 vol% Hellmanex III detergent in Milli-Q water, Milli-Q water and isopropanol, with intermediate rinsing with Milli-Q water. Substrates were immediately treated with an air plasma for 30 min before deposition of the compact blocking layer. TiO<sub>2</sub> blocking layers were spin coated from a solution of 0.37 mL titanium(IV) tetraisopropoxide, 35 μL of 2 M HCl in water, and 5 mL ethanol at 2000 rpm for 20 s before annealing at 150 ° for 30 min and sintering at 500 ° for 30 min<sup>1</sup>. SnO<sub>2</sub> blocking layers were spin coated from a solution of 17.5 mg/mL SnCl<sub>4</sub>·5H<sub>2</sub>O in anhydrous isopropanol at 2000 rpm before annealing at 100 ° for 30 min and 180 ° for 1 h. All spin coating treatments were carried out under a controlled environment with relative humidity of 20%. SnO<sub>2</sub> blocking layers were treated to a subsequent chemical bath

treatment containing 2500 mg urea, 2.5 mL 37% (w/v) HCl, 50 μL 3-mercaptopropionic acid and 540 mg SnCl<sub>2</sub>·2H<sub>2</sub>O in 200 mL Milli-Q water pre-heated to 70 °<sup>2</sup>. Chemical bath deposition was carried out for 2 h at 70 °, before rinsing with liberal amounts of water and again heating at 180° for 1 h.

Perovskite precursor solutions were weighed under an inert nitrogen atmosphere (<0.1% O<sub>2</sub>/H<sub>2</sub>O). Their composition was: MAPbI<sub>3</sub> where MA is methyl-ammonium, CH<sub>3</sub>NH<sub>3</sub>: 155.0 mg MAI + 481.0 mg PbI<sub>2</sub>; FAPbI<sub>3</sub> where FA is formamidinium, HC(NH<sub>2</sub>)<sub>2</sub>: 167.7 mg FAI + 481 mg PbI<sub>2</sub>; MAPbBr<sub>3</sub>: 109.2 mg MABr + 376.6 mg PbBr<sub>2</sub>. Precursors were engineered to contain ~6.8 mol% excess PbX<sub>3</sub><sup>3</sup>. Each precursor was dissolved in 0.75 mL of a pre-mixed 4:1 DMF:DMSO solution for 2 h before spin-coating. Antisolvent crystallisation method was used since it is applicable to all perovskite chemistries<sup>4,5</sup>. 70 μL of solution was deposited to the substrate before spun at 1000 rpm for 10 s and 4000 rpm for 30 s.<sup>1</sup>

### B. DFT simulation

Density functional theory (DFT) based calculations for the halide motion activation energies were performed using the CP2K code. The QUICKSTEP formalism<sup>6</sup> was employed where the Kohn-Sham orbitals were constructed by atom-centred DZVP Gaussian basis sets<sup>7</sup> and the electronic charge density in auxiliary plane wave basis sets with a 300 Ry energy cut-off. Analytical dual-space pseudopotentials and the generalised gradient approximation with the PBEsol form were adopted<sup>8</sup>. Additionally, we applied van der Waals interactions, as prescribed by Grimme *et al.* (DFT-D3)<sup>9</sup>. The nudged elastic band method in combination with the climbing image method was used to calculate the migration barrier for halogen atoms in the lattice<sup>10,11</sup>. We have considered the partial Schottky defect of AX (A=MA,FA, X=I,Br) to model the lattice with defects. To minimize the defect-defect interaction, we have considered a large enough (4 × 4 × 2 for MAPX<sub>3</sub> and 4 × 4 × 4 for FAPX<sub>3</sub>) supercell for these calculations.

<sup>a)</sup>Also at Faculty of Applied Sciences, Delft University of Technology, 2628 CJ Delft, The Netherlands

<sup>b)</sup>Also at Department of Chemistry, University of Bath, BA2 7AY, UK

### C. Drift-Diffusion Model

Iodide vacancies are constrained to the perovskite layer, with no generation or recombination. An equal, but static and uniformly-distributed, density of  $\text{MA}^+$  vacancies is included in the perovskite. Carrier generation occurs according to a Beer-Lambert profile. MAPI has an exciton binding energy much less than the thermal energy  $k_{\text{B}}T^{12,13}$ , so free charges are generated from each absorbed photon. Bulk recombination within the perovskite film is modelled using both direct band-to-band (bimolecular) relaxation and trap-based Shockley-Read-Hall (SRH) schemes. In SRH is a trap-based recombination scheme, where one carrier relaxes into a trap state within the bandgap, with which an opposite carrier later recombines<sup>14,15</sup>. The extent to which this mechanism occurs depends on the density and energy levels of mid-bandgap trap states, so will depend on the quality of the material. Bimolecular recombination, the reverse of photogeneration of carriers, takes place when an electron in the conduction band relaxes directly into a hole in the valence band. Free charge carriers in the electron and hole transport layers, ETL, HTL respectively, can recombine with an opposite carrier from the perovskite at the interface between the two materials in a process termed surface or interfacial recombination.

#### Model Symbols, parameter values and equations

Symbols and parameter values used in the model equations are shown in Tables I and II.

Symbol	Definition
$k_{\text{B}}$	Boltzmann constant, $8.62 \times 10^{-5} \text{ eV/K}$
$q$	Elementary charge, $1.60 \times 10^{-19} \text{ C}$
$\epsilon_0$	Permittivity of free space, $8.85 \times 10^{-12} \text{ F/m}$
$x$	Distance from ETL/perovskite interface
$t$	Time from start of simulation run
$\phi, \phi_E, \phi_H$	Electrostatic potential in the perovskite, ETL, HTL
$n, n_E$	Electron density in the perovskite, ETL
$p, p_H$	Hole density in the perovskite, HTL
$P$	Halide vacancy density in the perovskite
$F_n, F_{nE}$	Electron flux in the perovskite, ETL
$F_p, F_{pH}$	Hole flux in the perovskite, HTL
$F_P$	Halide vacancy flux in the perovskite
$G$	Generation in the perovskite
$R$	Bulk recombination in the perovskite
$R_{SE}$	Surface recombination at the perovskite/ETL interface
$R_{SH}$	Surface recombination at the perovskite/HTL interface

TABLE I. Symbols in the model equations and boundary conditions.

#### Perovskite layer, $0 < x < b$

Poisson and drift-diffusion equations for halide vacancies, electrons and holes:

$$\frac{\partial^2 \phi}{\partial x^2} = -\frac{q}{\epsilon}(P - N_0 + p - n) \quad (1)$$

$$\frac{\partial P}{\partial t} = -\frac{\partial F_P}{\partial x} \quad \text{where} \quad F_P = -D_P \left( \frac{\partial F_P}{\partial x} - \frac{P}{k_{\text{B}}T} \frac{\partial \phi}{\partial x} \right) \quad (2)$$

$$\frac{\partial n}{\partial t} = -\frac{\partial F_n}{\partial x} + G - R \quad \text{where} \quad F_n = -D_n \left( \frac{\partial n}{\partial x} + \frac{n}{k_{\text{B}}T} \frac{\partial \phi}{\partial x} \right) \quad (3)$$

$$\frac{\partial p}{\partial t} = -\frac{\partial F_p}{\partial x} + G - R \quad \text{where} \quad F_p = -D_p \left( \frac{\partial p}{\partial x} - \frac{p}{k_{\text{B}}T} \frac{\partial \phi}{\partial x} \right) \quad (4)$$

*Electron and Hole Transport Layers (ETL,HTL respectively)*  
The Poisson equation and the drift-diffusion equation for electrons in the ETL,  $-b_E < x < 0$ :

$$\frac{\partial^2 \phi_E}{\partial x^2} = -\frac{q}{\epsilon_E}(d_E - n_E) \quad (5)$$

$$\frac{\partial n_E}{\partial t} = -\frac{\partial F_{nE}}{\partial x} \quad \text{where} \quad F_{nE} = -D_{nE} \left( \frac{\partial n_E}{\partial x} + \frac{n_E}{k_{\text{B}}T} \frac{\partial \phi_E}{\partial x} \right) \quad (6)$$

As  $\text{TiO}_2$  does not absorb light, there are no generation nor recombination terms in (6). Holes to enter the ETL from the perovskite given the large energy barrier.

The Poisson equation and the drift-diffusion equation for holes in the HTL,  $b < x < b + b_H$ , are

$$\frac{\partial^2 \phi_H}{\partial x^2} = -\frac{q}{\epsilon_H}(p_H - d_H) \quad (7)$$

$$\frac{\partial p_H}{\partial t} = -\frac{\partial F_{pH}}{\partial x} \quad \text{where} \quad F_{pH} = -D_{pH} \left( \frac{\partial p_H}{\partial x} - \frac{p_H}{k_{\text{B}}T} \frac{\partial \phi_H}{\partial x} \right) \quad (8)$$

As for the ETL, there is no generation or recombination and the large energy barrier blocks electrons from entering the HTL.

#### Generation and recombination

Generation takes place within the perovskite layer only

$$G(x) = F_{ph}\alpha \exp(-\alpha x) \quad \text{for} \quad 0 < x < b \quad (9)$$

Bulk recombination sums trap-mediated Shockley-Read-Hall (SRH) and bimolecular (band to band)

$$R(n, p) = R_{\text{SRH}}(n, p) + R_{\text{Bimol}}(n, p) \quad (10)$$

where

$$R_{\text{SRH}}(n, p) = \frac{np - n_{\text{eq}}p_{\text{eq}}}{\tau_p(n + n_{\text{eq}}) + \tau_n(p + p_{\text{eq}})}, \quad (11)$$

$$R_{\text{Bimol}}(n, p) = \beta(np - n_{\text{eq}}p_{\text{eq}}), \quad (12)$$

$$n_{\text{eq}} = p_{\text{eq}} = n_i = g_c g_v \exp\left(-\frac{E_G}{2k_{\text{B}}T}\right) \dots \quad (13)$$

Surface recombination also occurs by an SRH mechanism

$$R_{\text{SE}}(n_E, p) = \frac{np - n_{\text{eq}}p_{\text{eq}}}{(n + n_{\text{eq}})/v_{nE} + \tau_n(p + p_{\text{eq}})/v_{pE}}. \quad (14)$$

Parameter	Symbol	Value
Temperature	$T$	300 K
Thermal voltage ( $= k_B T/q$ )	$V_T$	25.9 mV
<b>Properties of the perovskite layer</b>		
Width	$b$	400 nm <sup>16</sup>
Permittivity	$\epsilon$	$24.1 \epsilon_0$ <sup>17</sup>
Electron diffusivity	$D_n$	$1.7 \text{ cm}^2 \text{ s}^{-1}$ <sup>18</sup>
Hole diffusivity	$D_p$	$1.7 \text{ cm}^2 \text{ s}^{-1}$ <sup>18</sup>
Conduction band energy	$E_C$	-3.7 eV <sup>19</sup>
Valence band energy	$E_V$	-5.4 eV <sup>19</sup>
Bandgap ( $= E_C - E_V$ )	$E_G$	1.7 eV <sup>19</sup>
Conduction band density of states	$g_c$	$8.1 \times 10^{18} \text{ cm}^{-3}$ <sup>20</sup>
Valence band density of states	$g_v$	$5.8 \times 10^{18} \text{ cm}^{-3}$ <sup>20</sup>
Ion vacancy density	$N_0$	$1.6 \times 10^{19} \text{ cm}^{-3}$ <sup>17</sup>
High temperature ion diffusivity	$D_\infty$	$1.0 \times 10^{-3} \text{ cm}^2 \text{ s}^{-1}$ <sup>21</sup>
Activation energy for ion hop	$E_A$	0.58 eV <sup>21</sup>
<b>Properties of the electron transporting layer (ETL)</b>		
Width	$b_E$	50 nm
Permittivity	$\epsilon_E$	$40 \epsilon_0$
Electron diffusivity	$D_{nE}$	$1.5 \times 10^{-1} \text{ cm}^2 \text{ s}^{-1}$ <sup>16</sup>
Doping density	$d_E$	$1.7 \times 10^{18} \text{ cm}^{-3}$ <sup>16</sup>
Conduction band energy	$E_{FE}$	-3.95 eV <sup>19</sup>
<b>Properties of the hole transporting layer (HTL)</b>		
Width	$b_H$	200 nm
Permittivity	$\epsilon_H$	$3 \epsilon_0$
Hole diffusivity	$D_{pH}$	$1.5 \times 10^{-1} \text{ cm}^2 \text{ s}^{-1}$
Doping density	$d_H$	$8 \times 10^{17} \text{ cm}^{-3}$
HOMO energy	$E_{FH}$	-5.0 eV <sup>19</sup>
<b>Generation parameters</b>		
Incident photon flux (energy > $E_G$ )	$F_{ph}$	$1.4 \times 10^{17} \text{ cm}^{-2} \text{ s}^{-1}$
Perovskite absorptivity	$\alpha$	$1.3 \times 10^5 \text{ cm}^{-1}$ <sup>22</sup>
<b>Bulk recombination parameters</b>		
Bimolecular recomb. coefficient	$\beta$	$4.0 \times 10^{-5} \text{ cm}^3 \text{ s}^{-1}$
SRH electron pseudolifetime	$\tau_n$	$5.0 \times 10^{-12} \text{ s}$
SRH hole pseudolifetime	$\tau_p$	$5.0 \times 10^{-10} \text{ s}$
<b>Surface recombination parameters</b>		
Electron recomb. velocity at perov/ETL interface	$v_{nE}$	$1.0 \times 10^7 \text{ cm s}^{-1}$
Hole recomb. velocity at perov/ETL interface	$v_{pE}$	$100 \text{ cm s}^{-1}$
Electron recomb. velocity at perov/HTL interface	$v_{nH}$	$1.0 \text{ cm s}^{-1}$
Hole recomb. velocity at perov/HTL interface	$v_{pH}$	$1.0 \times 10^7 \text{ cm s}^{-1}$

TABLE II. Parameter symbols and values used except where indicated in the figure captions. Most parameters are consistent with<sup>16</sup> given that the same model was used here. Courtier et al<sup>16</sup> explored the consequences for  $H$  and the accumulated ion charge density adjacent to the ETL of varying  $d_E$ ,  $d_H$  and  $\epsilon_E$ . The values of  $\tau_n$  and  $\tau_p$  are 6 times smaller than those used in Set (a) of<sup>16</sup> to allow for the lower efficiencies of our measured cells compared to the modelled cells of<sup>16</sup>. In a later publication<sup>23</sup>, Courtier et al investigated the sensitivity of charge extraction to this parameter set. The temperature variation of the ion vacancy density  $N_{ion} = N_0 \exp[0.5\Delta H_S/(k_B T)]$  where  $\Delta H_S$  is the formation energy of a Schottky defect pair has been neglected here since  $0.5 \Delta H_S \ll E_A$ .

$$R_{SH}(p_H, n) = \frac{np - n_{eq}p_{eq}}{(n + n_{eq})/v_{nH} + (p + p_{eq})/v_{pH}}. \quad (15)$$

Fixed electron density at the left electrode.

$$n_E = d_E \quad (17)$$

### Boundary Conditions

*Electrode/ETL interface* ( $x = -b_E$ )

The total voltage across the cell is  $V_{bi} - V_{ap}$ . This potential difference is divided equally between the potentials at the left and right electrodes.

$$\phi_E = \frac{(V_{bi} - V_{ap})}{2} \quad (16)$$

*ETL/perovskite interface*,  $x = 0$

Continuity of the potential and electric displacement across the interface

$$\phi_E = \phi, \epsilon \frac{\partial \phi}{\partial x} = \epsilon_E \frac{\partial E}{\partial x} \quad (18)$$

Halide ions may not leave the perovskite.

$$F_P = 0 \quad (19)$$

Conservation of electron flux (and therefore charge), taking account of surface recombination. and

$$F_{nE} = F_n + R_{SE} \quad (20)$$

Electron density across the energy barrier

$$n_E = n \frac{d_E}{g_c} \exp\left(\frac{E_C - E_{FE}}{k_B T}\right) \quad (21)$$

Holes can not transfer to the ETL from the perovskite so the only flux towards this interface is recombination flux.

$$-F_p = R_{SE} \quad (22)$$

*Perovskite/HTL interface,  $x = b$*

Continuity of potential and electric displacement field.

$$\phi = \phi_H, \quad \epsilon \frac{\partial \phi}{\partial x} = \epsilon_H \frac{\partial \phi_H}{\partial x} \quad (23)$$

Eq (19) also holds at this interface. Conservation of hole flux

$$F_p = F_{pH} - R_{SH} \quad (24)$$

Hole density across the energy barrier

$$p_H = p \frac{d_H}{g_v} \exp\left(\frac{E_{FH} - E_V}{k_B T}\right) \quad (25)$$

Electrons can not transfer to the HTL from the perovskite so the only flux towards this interface is recombination flux.

$$F_n = R_{SH} \quad (26)$$

*HTL/Electrode interface,  $x = b + b_H$*

$$\phi_H = -\frac{(V_{bi} - V_{ap})}{2} \quad (27)$$

Fixed hole density at the right electrode.

$$p_H = d_H \quad (28)$$

<sup>1</sup>J. M. Ball, M. M. Lee, A. Hey, and H. J. Snaith, “Low-temperature processed meso-superstructured to thin-film perovskite solar cells,” *Energy Environ. Sci.* **6**, 1739–1743 (2013).

<sup>2</sup>E. H. Anaraki, A. Kermanpur, L. Steier, K. Domanski, T. Matsui, W. Tress, M. Saliba, A. Abate, M. Grätzel, A. Hagfeldt, and J.-P. Correa-Baena, “Highly efficient and stable planar perovskite solar cells by solution-processed tin oxide,” *Energy Environ. Sci.* **9**, 3128–3134 (2016).

<sup>3</sup>D. Bi, W. Tress, M. I. Dar, P. Gao, J. Luo, C. Renévier, K. Schenk, A. Abate, F. Giordano, J.-P. Correa Baena, J.-D. Decoppet, S. M. Zakeeruddin, M. K. Nazeeruddin, M. Grätzel, and A. Hagfeldt, “Efficient luminescent solar cells based on tailored mixed-cation perovskites,” *Sci. Adv.* **2** (2016).

<sup>4</sup>M. Xiao, F. Huang, W. Huang, Y. Dkhissi, Y. Zhu, J. Etheridge, A. Gray-Weale, U. Bach, Y.-B. Cheng, and L. Spiccia, “A fast deposition-crystallization procedure for highly efficient lead iodide perovskite thin-film solar cells,” *Angew. Chem.* **126**, 10056–10061 (2014).

<sup>5</sup>M. Saliba, T. Matsui, J.-Y. Seo, K. Domanski, J.-P. Correa-Baena, M. K. Nazeeruddin, S. M. Zakeeruddin, W. Tress, A. Abate, A. Hagfeldt, and M. Grätzel, “Cesium-containing triple cation perovskite solar cells: improved stability, reproducibility and high efficiency,” *Energy Environ. Sci.* **9**, 1989–1997 (2016).

<sup>6</sup>J. VandeVondele, M. Krack, F. Mohamed, M. Parrinello, T. Chassaing, and J. Hutter, “QUICKSTEP: Fast and accurate density functional calculations using a mixed Gaussian and plane waves approach,” *Comput. Phys. Commun.* **167**, 103 – 128 (2005).

<sup>7</sup>J. VandeVondele and J. Hutter, “Gaussian basis sets for accurate calculations on molecular systems in gas and condensed phases,” *J. Chem. Phys.* **127**, 114105 (2007).

<sup>8</sup>J. P. Perdew, K. Burke, and M. Ernzerhof, “Generalized gradient approximation made simple,” *Phys. Rev. Lett.* **77**, 3865–3868 (1996).

<sup>9</sup>S. Grimme, J. Antony, S. Ehrlich, and H. Krieg, “A consistent and accurate *ab initio* parametrization of density functional dispersion correction (DFT-D) for the 94 elements H-Pu,” *J. Chem. Phys.* **132**, 154104 (2010).

<sup>10</sup>G. Mills, H. Jónsson, and G. K. Schenter, “Reversible work transition state theory: application to dissociative adsorption of hydrogen,” *Surf. Sci.* **324**, 305 – 337 (1995).

<sup>11</sup>G. Henkelman, B. P. Uberuaga, and H. Jónsson, “A climbing image nudged elastic band method for finding saddle points and minimum energy paths,” *J. Chem. Phys.* **113**, 9901–9904 (2000).

<sup>12</sup>Q. Lin, A. Armin, R. C. R. Nagiri, P. L. Burn, and P. Meredith, “Electro-optics of perovskite solar cells,” *Nat. Photon.* **9**, 106–112 (2015).

<sup>13</sup>A. Miyata, A. Mitioglu, P. Plochocka, O. Portugall, J. T.-W. Wang, S. D. Stranks, H. J. Snaith, and R. J. Nicholas, “Direct measurement of the exciton binding energy and effective masses for charge carriers in organic-inorganic tri-halide perovskites,” *Nat. Phys.* **11**, 582–587 (2015).

<sup>14</sup>W. Shockley and W. T. Read Jr., “Statistics of the recombinations of holes and electrons,” *Phys. Rev.* **87**, 835–842 (1952).

<sup>15</sup>R. N. Hall, “Electron-hole recombination in germanium,” *Phys. Rev.* **87**, 387 (1952).

<sup>16</sup>N. E. Courtier, J. M. Cave, J. M. Foster, A. B. Walker, and G. Richardson, “How transport layer properties affect perovskite solar cell performance: insights from a coupled charge transport/ion migration model,” *Energy Environ. Sci.* **12**, 396–409 (2019).

<sup>17</sup>A. Walsh, D. O. Scanlon, S. Chen, X. G. Gong, and S.-H. Wei, “Self-regulation mechanism for charged point defects in hybrid halide perovskites,” *Angew. Chem. Int. Ed.* **127**, 1811 (2015).

<sup>18</sup>C. C. Stoumpos, C. D. Malliakas, and M. G. Kanatzidis, “Semiconducting tin and lead iodide perovskites with organic cations: Phase transitions, high mobilities, and near-infrared photoluminescent properties,” *Inorg. Chem.* **52**, 9019–9038 (2013).

<sup>19</sup>P. Schulz, E. Edri, S. Kirmayer, G. Hodes, D. Cahen, and A. Kahn, “Interface energetics in organo-metal halide perovskite-based photovoltaic cells,” *Energy Environ. Sci.* **7**, 1377–1381 (2014).

<sup>20</sup>F. Brivio, K. T. Butler, A. Walsh, and M. van Schilfgaarde, “Relativistic quasiparticle self-consistent electronic structure of hybrid halide perovskite photovoltaic absorbers,” *Phys. Rev. B* **89**, 155204 (2014).

<sup>21</sup>C. Eames, J. M. Frost, P. R. F. Barnes, B. C. O'Regan, A. Walsh, and M. S. Islam, “Ionic transport in hybrid lead iodide perovskite solar cells,” *Nat. Commun.* **6**, 7497 (2015).

<sup>22</sup>P. Löper, M. Stuckelberger, B. Niesen, J. Werner, M. Filipič, S.-J. Moon, J.-H. Yum, M. Topič, S. De Wolf, and C. Ballif, “Complex refractive index spectra of  $\text{CH}_3\text{NH}_3\text{PbI}_3$  perovskite thin films determined by spectroscopic ellipsometry and spectrophotometry,” *J. Phys. Chem. Lett.* **6**, 66–71 (2015).

<sup>23</sup>N. E. Courtier, G. Richardson, and J. M. Foster, “A fast and robust numerical scheme for solving models of charge carrier transport and ion vacancy motion in perovskite solar cells,” *Appl. Math. Model.* **63**, 329–348 (2018).

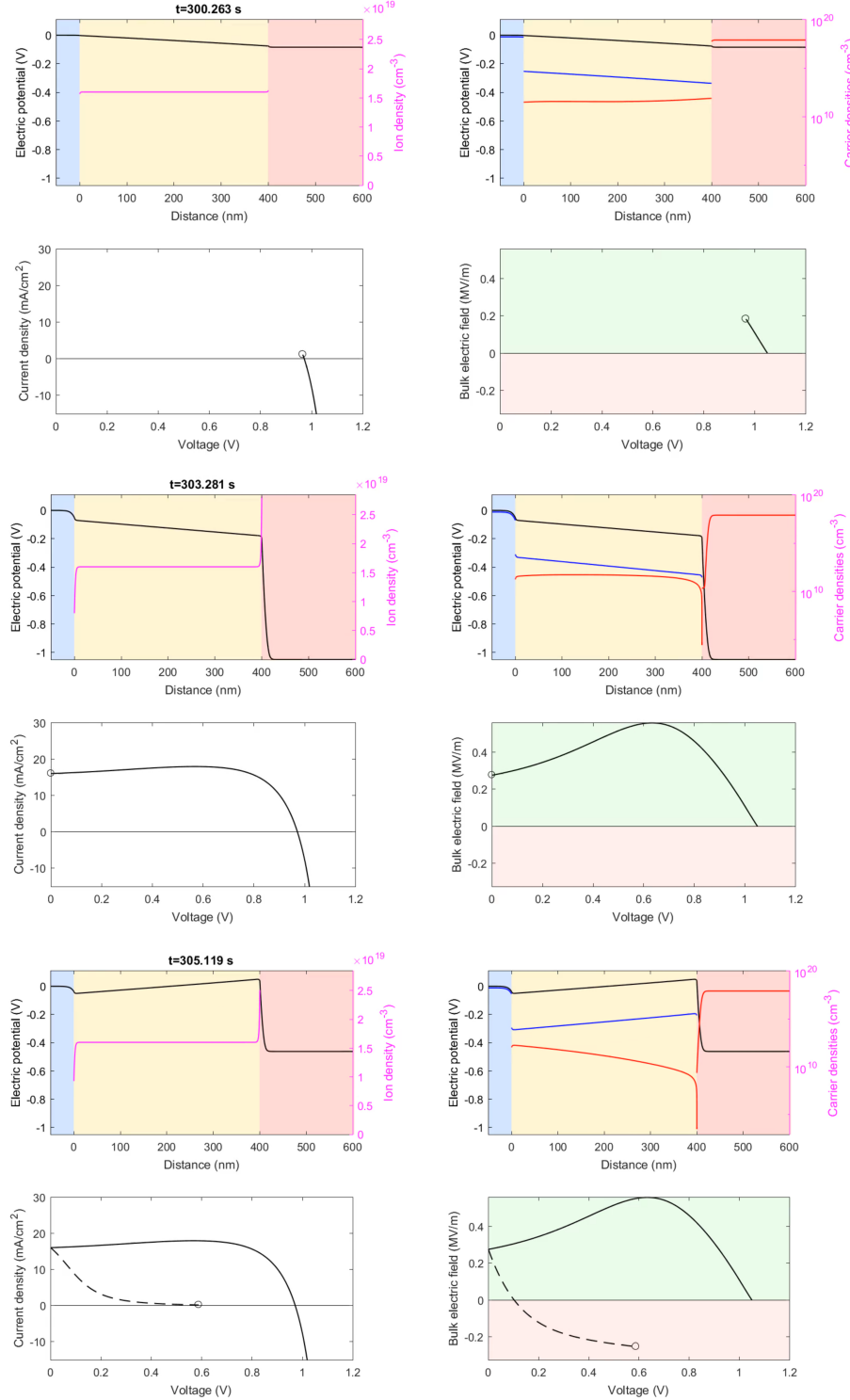


FIG. 1. Stills from Supplementary Video 2 for a scan rate of 320 mV/s used for the  $J$ - $V$  curve in Figure 2b. Each set of 4 panels is for a simulated planar device ETL(blue,  $\text{TiO}_2$ ) /perovskite (yellow, MAPI)/HTL (pink, spiro) at a time  $t$  since the start of the simulation. Applied bias is  $V_{\text{oc}}$  in the reverse scan (top 4 panels), zero (middle 4 panels),  $V_{\text{oc}}$  in the forward scan (bottom 4 panels).

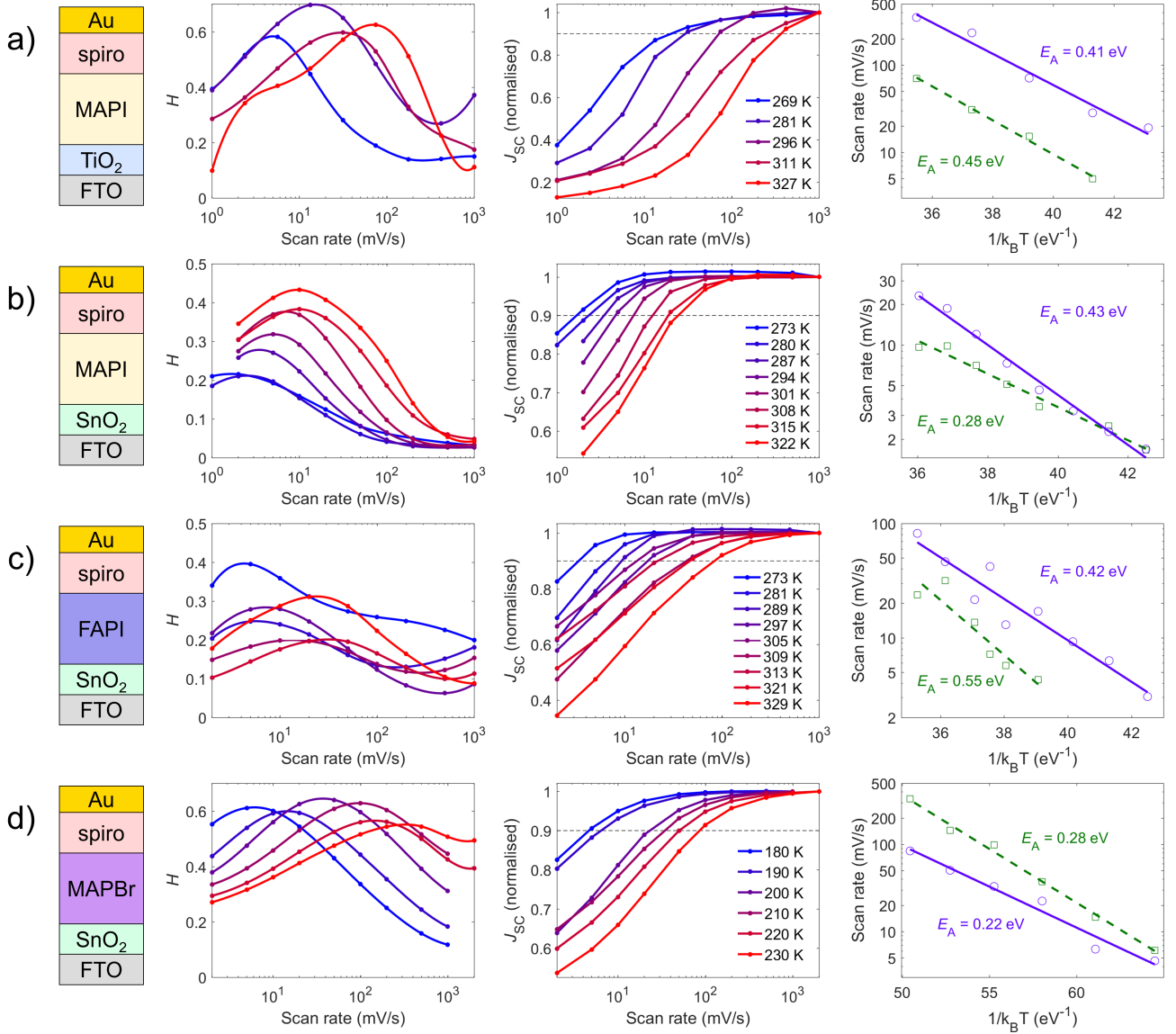


FIG. 2. Left column schematic diagrams of (a) TiO<sub>2</sub>/MAPI, (b) SnO<sub>2</sub>/MAPI, (c) SnO<sub>2</sub>/FAPI and (d) SnO<sub>2</sub>/MAPbBr<sub>3</sub> devices. Second and third columns respectively hysteresis factor  $H$  and  $J_{sc}$  vs scan rate as the temperature  $T$  varies from 270 to 310 K in steps of 10 K. The rightmost column shown in Figure 5 of the main text gives Arrhenius fits of the measured scan rate yielding 90% of maximum  $J_{sc}$  (purple circles, solid lines) and maximum hysteresis factor  $H$  (green squares, dashed lines).  $E_A$  is obtained from the gradient of each line, labelled on each plot, and listed in Table 1. Digitisation of the voltages applied by the potentiostat with a minimum step size of 10 mV leads to errors of a few mA/cm<sup>2</sup> in the  $J_{sc}$  values in the second column. For consistency, the  $J_{sc}$  value from the reverse scan was used to deduce the scan rate giving 90%  $J_{scmax}$  by interpolation. The error in this scan rate arising from the small number of data points affected by the digitization is reduced through the Arrhenius plot smoothing out these errors through the slope fit used to deduce the activation energy  $E_A$  in Figure 5 of the main paper.

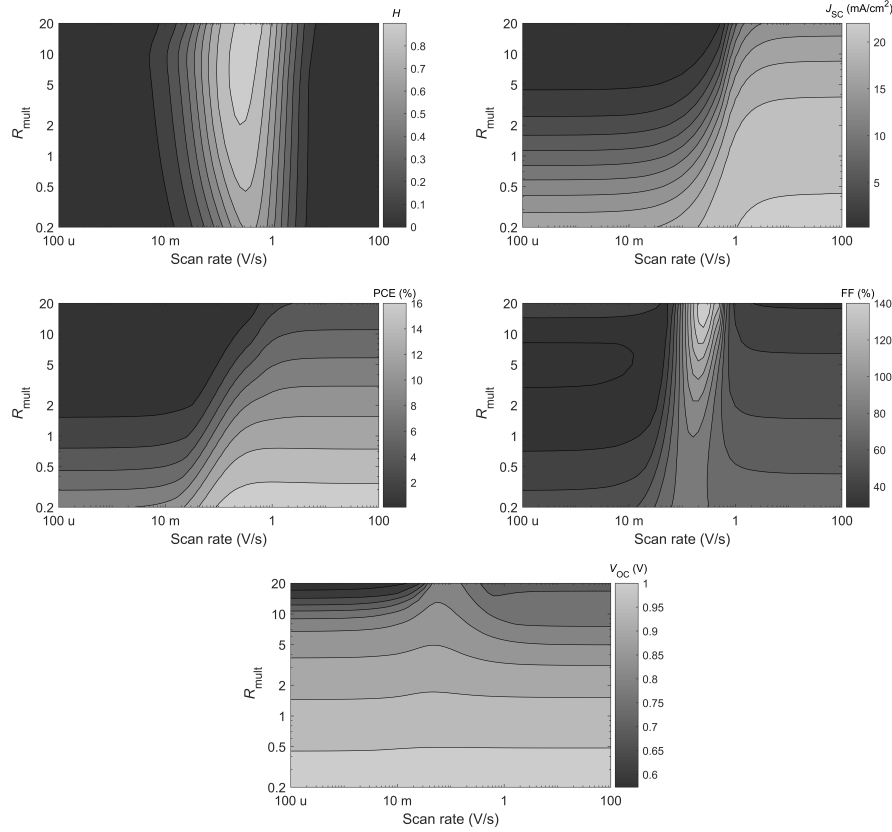


FIG. 3. Variation of  $H$ ,  $J_{sc}$ , PCE, FF and  $V_{oc}$  with the recombination multiplier  $R_{mult}$  which multiplies the bimolecular recombination coefficient  $\beta$  and the surface recombination velocities  $v_{nE}$ ,  $v_{pE}$ ,  $v_{nH}$  and  $v_{pH}$  and divides the electron and hole SRH pseudolifetimes  $\tau_n$  and  $\tau_p$ . For the other figures,  $R_{mult} = 1$ . The timescale of hysteresis and current loss is largely unchanged with increasing recombination, while the loss becomes more severe.

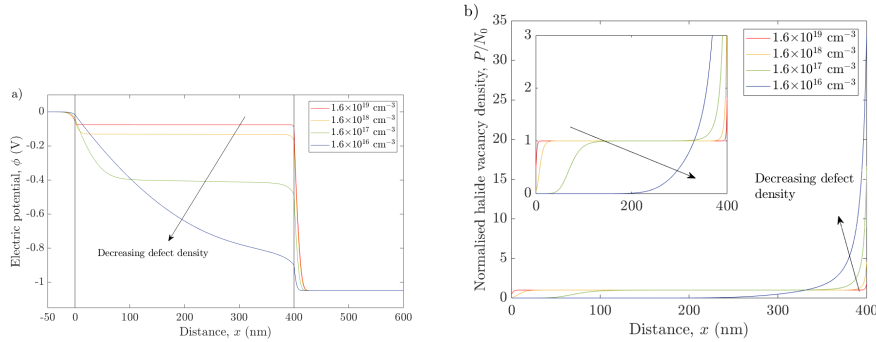


FIG. 4. The simulated distribution of (a) the electric potential across the ETL, perovskite and HTL, and (b) the normalised ion vacancy distribution across the perovskite, at short-circuit during a very slow (1 mV/s)  $J$ - $V$  scan for the 4 defect densities shown in the legend. Reducing the defect density causes the proportion of the total potential drop lying within the perovskite layer to increase<sup>16</sup>. It also causes the Debye length to increase so the electric fields around each interface extend further into the perovskite. For the lowest defect density, there is a positive electric field across the entire width of the perovskite layer (even at steady state). This field causes enhanced charge separation and thus improved cell performance (particularly for a cell limited by recombination in the bulk of the perovskite, as simulated here). Note that the width of the Debye layer on the left-hand side of the perovskite increases far more than that on the right-hand side due to the relatively small density of vacant ion sites that can be filled. In contrast, ion vacancies are able to accumulate at a much higher density, and therefore in a much narrower layer, adjacent to the perovskite/HTL interface.